

The SHMS 11GeV/c Spectrometer in Hall C at Jefferson Lab

S. Ali^a, A. Asaturyan^b, P. Brindza^c, M. Carmignotto^a, A. Dittmann^f, D. Dutta^d, R. Ent^c, H. Fenker^{c,*}, M. Fowler^c, N. Hlavin^a, T. Horn^{a,c}, Y. Illieva^e, S. Lassiter^c, A. Mkrtchyan^a, H. Mkrtchyan^b, P. Nadel-Turonski^c, I. Pegg^a, A. Ramos^g, J. Reinhold^g, I. Sapkota^a, V. Tadevosyan^b, S. Zhamkochyan^b, S. A. Wood^c

^a*The Catholic University of America, Washington, DC 20064, USA*

^b*A. I. Alikhanyan National Science Laboratory, Yerevan 0036, Armenia*

^c*Thomas Jefferson National Accelerator Facility, Newport News, Virginia 23606, USA*

^d*Mississippi State University, Mississippi State, Mississippi 39762, USA*

^e*University of South Carolina, Columbia, South Carolina 29208, USA*

^f*University of Illinois, Urbana-Champaign, Illinois, USA*

^g*Florida International University, University Park, Florida 33199, USA*

^h*Physics Division, Thomas Jefferson National Accelerator Facility, Newport News, VA. 23606, USA*

Abstract

The *Super High Momentum Spectrometer* (SHMS) has been built for Hall C at the Thomas Jefferson National Accelerator Facility (Jefferson Lab). With a momentum capability reaching 11 GeV/c, the SHMS provides measurements of secondary charged particles produced in electron scattering experiments using the maximum available beam energy from the upgraded Jefferson Lab accelerator. The SHMS comprises an array of triggering, tracking, and particle-identificaiton detectors that analyze particles transported and focused by a series of superconducting magnets, an optimized shielding enclosure, high-speed triggering and data-acquisition systems, and a carraige that supports it all. With a large acceptance over scattering angles from 5.5° to 40°, a wide range of low cross-section experiments may be performed. Some of these will complement and extend the previous successful Hall-C physics program to higher energies, and some will explore new physics.

Keywords: Magnetic spectrometer, Electron scattering, Tracking detectors, Particle identification, Electron calorimetry, Radiation shielding.

1. Introduction

2 Introduction section. Author Organizer: D. Gaskell

3 1.1. Jefferson Lab Overview

4 Originally 4 GeV → 6 GeV. Capabilities: Energy,
5 currents, polarization. Overall JLab program: Comple-
6 mentarity of 3 halls.

7 12 GeV Upgrade: New hall D. Hall A → upgraded
8 beamline, large installations. Halls B and C → new
9 spectrometers.

10 1.2. Hall C Experimental Program at 6 GeV

11 Standard equipment: HMS and SOS.

12 Notable (standard equipment) results from Hall C 6
13 GeV:

14 1. Inclusive cross sections → duality

15 2. Inclusive L-T separations

16 3. Exclusive meson production, with L-T separations.

17 4. SIDIS

18 5. $x > 1$, EMC Effect

19 6. Color Transparency

20 Figures (2-4): Duality, Inclusive L-Ts, Fpi, $x \geq 1$

21 1.3. Hall C 12 GeV Program

22 The new, Super-High Momentum Spectrometer was
23 designed to build on the experimental capabilities ex-
24 ploited during the Hall C program at higher energies.
25 Notably, this includes:

26 1. Excellent kinematic control reproducibility

27 2. Thorough understanding of spectrometer accep-
28 tance

29 3. Small angle capability (down to 5.5 degrees) for
30 detection of forward mesons

*Corresponding author

- 31 4. Central momentum up to (nearly) the maximum
32 beam energy accessible in Hall C
33 5. In-plane and out-of-plane acceptance well matched
34 to the existing HMS to facilitate experiments de-
35 tecting two particle in coincidence

36 Describe experiments and relevance of each feature:
37 Inclusive cross sections: Kinematics, acceptance. Me-
38 son electroproduction (LT): Kinematics, acceptance,
39 forward angle detection Color transparency and $xx > 1$:
40 Large central momentum

41 Projections from proposals: Perhaps use Commission-
42 ing Experiments since they were chosen to exercise
43 SHMS capabilities.

44 2. Specifications for the upgraded Hall-C Spectrom- 45 eter

46 SHMS Specifications section. Author Organizer: H. 47 Fenker

48 The physics outlined in the previous section can be
49 accessed only if the Hall C spectrometer system is capa-
50 ble of providing the necessary measurements with preci-
51 sion, rate, and trigger capabilities consistent with those
52 physics goals. Originally, Hall C offered the 7.4 GeV/c
53 High Momentum Spectrometer (HMS) and its lower-
54 momentum (1.8 GeV/c) partner, the Short-Orbit Spec-
55 trometer (SOS). These two devices were utilized inde-
56 pendently by some experiments and in coincidence by
57 others. The performance specifications for the SHMS
58 were drafted such that the SHMS-HMS pair would pro-
59 vide similar complimentary functions in the higher-
60 momentum regime. That is, the SHMS was developed
61 as a general-purpose spectrometer with properties simi-
62 lar to the existing HMS, but with a higher maximum
63 momentum capability (11 GeV/c). Table 1 summarizes
64 the demonstrated performance of the HMS and the de-
65 sign specifications for the SHMS.

66 With the higher beam energies in use at Jefferson Lab
67 after the 12-GeV Upgrade, scattered electrons and sec-
68 ondary particles are boosted to more forward directions.
69 Thus the SHMS acceptance is made to extend down
70 to a 5.5° scattering angle, and needs to cover angles
71 no higher than 40° . Nevertheless, high energies gen-
72 erally lead to smaller cross sections. Therefore preci-
73 sion experiments can be performed only if a spectrom-
74 eter provides large overall acceptance, high rate capa-
75 bility, and precise momentum measurement. As shown
76 in Table 1, the SHMS design includes a momentum bite
77 even larger than the HMS, and achieves an angular ac-
78 ceptance within a factor of two of its low-energy part-
79 ner. The combination of dispersive optics and preci-

80 sion tracking provides excellent momentum resolution.
81 Triggering, data-acquisition, and particle identification
82 rates are the same or better than those of the HMS. This
83 performance is achieved not only through the use of
84 faster, modern electronics, but also by innovative radia-
85 tion shielding that reduces the background flux seen by
86 the detectors.

87 3. Design and Development of the SHMS Systems

88 In this section we present design details and data
89 demonstrating the performance of each the SHMS sub-
90 systems. The entire spectrometer is carried on a steel
91 support structure which can rotate through an arc on the
92 left side of the beam-line in Hall C. Like the HMS car-
93 riage, it is secured to a central pivot so that it rotates
94 around a vertical axis that intersects the electron beam-
95 line at the experimental target. This is shown in Fig. 1.

96 Acceptance at the smallest scattering angles is en-
97 abled by the presence of a horizontal-bending dipole as
98 the first element in the magnetic optical system. This
99 small deflection moves the subsequent pieces of the
100 SHMS farther from the beamline, relaxing the size con-
101 straints on the other magnetic elements (described in
102 Section 3.1) and shielding (Section 3.2). The shielded
103 enclosure is itself a technically-optimized combination
104 of concrete, lead, boron, and plastic. It surrounds the
105 detectors and the electronics of the control and data-
106 acquisition systems.

107 Basic trigger information comes from four planes
108 of scintillator or quartz-bar hodoscopes. Tracking is
109 provided by twelve planes of conventional drift cham-
110 bers, and particle identification uses gas and aerogel
111 Čerenkov counters, a preshower counter, and a total-
112 absorption shower counter. The detector system details
113 are presented in sections 3.3 through 3.9. Details of the
114 event-triggering schemes, the data-acquisition system,
115 and software appear in sections 3.10 and 3.11.

116 Editing notes.

117 The subsections below (numbered 3.xx) are each as-
118 signed to a technical subsystem author (or organizer), as
119 indicated. The order of these subsections has not been
120 given any thought yet. Each one should describe design
121 and performance objectives, studies and test results that
122 lead to the design choices, a description of the final de-
123 sign (here you might include pertinent drawings), and
124 the results of bench-top or in-beam commissioning re-
125 sults that demonstrate how well the detector works (effi-
126 ciency, photoelectron yield, pedestal width, timing res-
127 olution, or whatever is relevant for characterizing your
128 piece of hardware).

<i>Parameter</i>	<i>HMS Performance</i>	<i>SHMS Specification</i>
Range of Central Momentum	0.4 to 7.4 GeV/c	2 to 11 GeV/c
Momentum Acceptance	$\pm 10\%$	-10% to +22%
Momentum Resolution	0.1% – 0.15%	0.03% – 0.08%
Scattering Angle Range	10.5° to 90°	5.5° to 40°
Target Length Accepted at 90°	10 cm	50 cm
Horizontal Angle Acceptance	± 32 mrad	± 18 mrad
Vertical Angle Acceptance	± 85 mrad	± 50 mrad
Solid Angle Acceptance	8.1 msr	>4 msr
Horizontal Angle Resolution	0.8 mrad	0.5 – 1.2 mrad
Vertical Angle Resolution	1.0 mrad	0.3 – 1.1 mrad
Target resolution (ytar)	0.3 cm	0.1 - 0.3 cm
Maximum Event Rate	2000 Hz	10,000 Hz
Max. Flux within Acceptance	~ 5 MHz	~ 5 MHz
e/h Discrimination	>1000:1 at 98% efficiency	>1000:1 at 98% efficiency
π/K Discrimination	100:1 at 95% efficiency	100:1 at 95% efficiency

Table 1: Demonstrated Performance of the HMS and Design Specifications for the SHMS

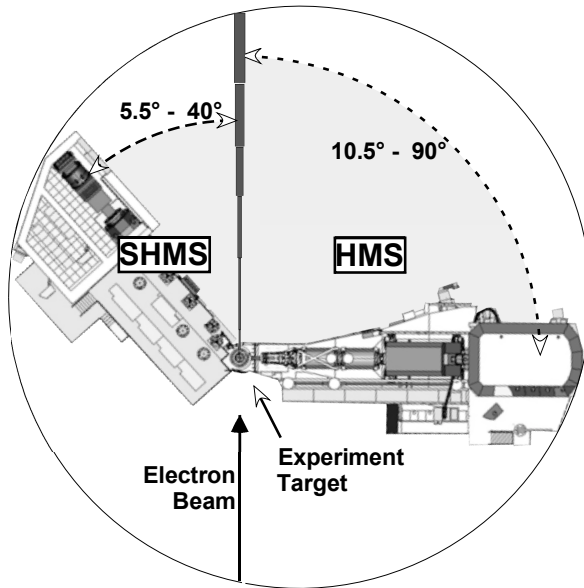


Figure 1: Simplified Plan View of Hall C showing the footprints of the SHMS and HMS. The SHMS occupies the smaller side of Hall C, where the smaller, low-momentum Short-Orbit Spectrometer (SOS) had been previously located.

3.1. Magnetic Optics

Magnetic Optics section. Author Orgainzer: M. Jones

When beam electrons scatter in the experimental target, secondary particles are produced over a wide range of directions and energies. Those possessing a product of electric charge and momentum that is close to that for which the spectrometer is configured will be *accepted*: they will pass through the spectrometer and will be sensed by the array of particle detectors.

The charged-particle optics of the SHMS provides a point-to-point focus using a quadrupole triplet. To optimize acceptance in the vertical scattering plane, the first quadrupole focuses in the vertical while the second quadrupole defocuses and the third quadrupole focuses. A vertical-bending dipole magnet follows the last quadrupole and disperses particles with different momenta across the focal plane. In point-to-point optics, all particles with the same momentum will be displaced by the same vertical distance in the focal plane.

3.1.1. The Magnets and Vacuum Channel

A specially-design horizontal-bend dipole (HB) precedes the first quadrupole. Its purpose is to provide an initial 3° separation between scattered particles and the electron beam so that particles scattered at small angles can be accepted.

As shown in Fig. 1, in order to fit within the space available in Hall C the SHMS must be even shorter than its lower-momentum partner, the HMS. All of the SHMS magnets are superconducting so that they can

provide the necessary large bending and focusing effects in short distances. Given the small-angle acceptance requirement, the HB and the first two quadrupoles (Q1 and Q2) must have special provisions to provide clearance for the electron beam and its vacuum pipe. HB is a "C"-magnet so that all of the flux-return iron is on the side away from the beamline. The front of the HB cryostat, between the beamline and the magnet bore, is made very narrow. Both Q1 and Q2 have notches in their cryosats and iron yokes so that they, too, can clear the beamline when the spectrometer is configured at small scattering angles. Yoke steel for Q1 is inside the cryostat. The other magnets, including the final quadrupole (Q3) and the dipole (D_{SHMS}) have external, warm, yokes. Parameters of the SHMS magnets are provided in Table 2. Details about the design and construction of the SHMS magnets can be found in [3].

To minimize multiple scattering as particles pass through the SHMS, the bores of all of the magnets are evacuated. The vacuum space begins at a window on the front of HB and extends either to the exit of D_{SHMS} or, through a Vacuum Extension Tank (VET), to within 30 cm of the first drift chamber in the detector stack. The entrance window into HB is approximately 15 cm square, while the vacuum vessel bore through Q2, Q3, and (D_{SHMS}) is 60 cm in diameter.

185 3.1.2. Optics

The relative strengths of the integral fields of the magnets are set to maximize acceptance while at the same time optimizing resolution in momentum and scattering angle. The transport of a particle with the relative momentum, $\delta = \frac{p-p_c}{p_c}$, from the target to midway between the two set drift chambers in the focal plane of the SHMS can be characterized by an optics matrix. The particle momentum is p and the central momentum of the spectrometer is p_c . The particle starts with the vertical and horizontal positions (x_{tar} and y_{tar}) and angles ($x'_{tar} = \frac{\Delta x_{tar}}{\Delta z_{tar}}$ and $y'_{tar} = \frac{\Delta y_{tar}}{\Delta z_{tar}}$) in the $z_{tar} = 0$ plane. These positions and angles are measured relative to the central ray of the spectrometer. After magnetic transport, it arrives at the focal plane with the vertical and horizontal positions (x_{fp} and y_{fp}) and angles (x'_{fp} and y'_{fp}). The first order optics matrix is

$$\begin{pmatrix} x_{fp} \\ x'_{fp} \\ y_{fp} \\ y'_{fp} \end{pmatrix} \begin{pmatrix} -1.36 & 0.0 & 0.0 & 0.04 & 1.623 \\ -0.07 & -0.73 & 0.0 & 0.0 & 0.32 \\ 0.0 & 0.01 & -1.634 & 0.0 & -0.19 \\ 0.0 & -0.27 & -0.27 & -0.61 & 0.0 \end{pmatrix} \begin{pmatrix} x_{tar} \\ x'_{tar} \\ y_{tar} \\ y'_{tar} \\ \delta \end{pmatrix} = \begin{pmatrix} 232 \\ 233 \\ 234 \\ 235 \\ 236 \end{pmatrix} \quad (1)$$

¹⁸⁶ The units of the positions are in meters.

The acceptance of the spectrometer is mainly determined by the collimator that is placed between the HB magnet and the first quadrupole. A remotely-operated collimator box is installed on the SHMS between the HB and Q1 magnets. The collimator ladder assembly within this box may be positioned at three settings. The top position (accessed when the assembly is at its lowest position) is a stretched octagon with opening height 9.843" and width 6.693" on the upstream side. It is 2.5" thick. The lower two positions both present sieve holes in rectangular pattern with holes separated by 0.6457" horizontally and 0.9843" vertically. The sieve pattern at the middle ladder position has 11 columns of holes with the sixth column centered horizontally. The holes on the bottom sieve are in ten columns and are offset by one-half a column gap from those in the middle sieve. The sieve collimators are 1.25" thick. The geometry is illustrated in Fig. 2. Both sieves and octagonal collimator are made of Mi-Tech™ Tungsten HD-17 (Density 17 g/cc, 90% W, 6% Ni, 4% Cu).

To determine the vertical size of the collimator studies were done with SNAKE (magnet transport code). Without the collimator, the vertical acceptance is mainly determined by the mechanical exit of the HB magnet. The vertical size of ± 12.5 cm was chosen to match this vertical cut-off to maximize the acceptance. Two vertical sizes of ± 8 cm and ± 10.5 cm for the collimators were studied. A plot of the acceptance each collimator versus δ is shown in Figure 3. The acceptance drops from an average of 4 msr for ± 12.5 cm to an average of 3 msr for ± 8 cm. Another consideration minimizing the loss of events in the bore of the vertical dipole after they pass the entrance of the dipole. A plot in Figure 3 shows the fraction of events which make it to the focal plane. The number of events lost in the dipole bore as a function of δ is reduced by decreasing the vertical height of the collimator. With the ± 12.5 cm collimator, the fraction of events making to the focal plane drops to 75% at $\delta = 0.15$. The decision was made to use the ± 12.5 cm vertical opening to maximize the solid angle acceptance of the SHMS at the expense of increased reliance on the understanding the losses in the SHMS dipole bore.

A magnetic transport code, SNAKE, was used to model the acceptance of the SHMS. The mechanical sizes of the magnets and magnet field maps from TOSCA are used to create a model of the SHMS in SNAKE. The acceptance of the SHMS versus δ determined by SNAKE is plotted in Fig. 4. A separate calculation is done using the Hall C Monte Carlo (SIMC) which uses COSY transport matrix. The acceptance of the SHMS versus δ determined by SIMC is plotted in Fig. 4. The agreement between the two calculations is

<i>Parameter</i>	<i>HB</i>	<i>Q1</i>	<i>Q2</i>	<i>Q3</i>	<i>D_{SHMS}</i>
Max Field or Gradient	2.6 T	7.9 T/m	11.8 T/m	7.9 T/m	3.9 T
Effective Field Length	0.75 m	1.9 m	1.6 m	1.6 m	2.9 m
Current at 11 GeV/c	3923 A	2322 A	3880 A	2553 A	3510 A
Aperture	14.5x18 cm	40 cm	60 cm	60 cm	60 cm

Table 2: Parameters of the SHMS Magnets

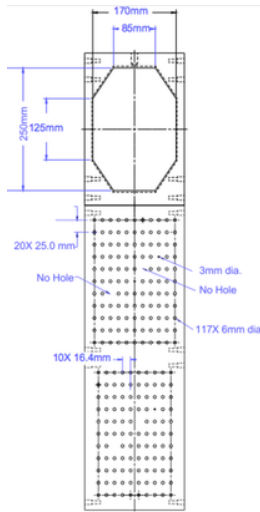


Figure 2: SHMS collimator

excellent.

The reconstruction of particle's momentum, horizontal target position and vertical and horizontal angles from the focal plane positions and angles can also be represented by an optics matrix. [Need to complete this. M. Jones](#)

Calibration of the δ matrix was done using carbon elastic data. [Need to complete this. Will add part about the ytar,yptar and xptar calibration M. Jones](#)

3.2. Shield House Layout, Shielding Design

[Shield House layout and materials section. Author Organizer: T. Horn](#)

The radiation environment is an important consideration for the design of the SHMS shield house, in partic-

ular, the effect of radiation-induced effects on the performance and reliability of detectors and electronics. It has been shown that many new commercial off the shelf components are more sensitive to radiation damage and single event upsets, requiring a careful evaluation of the impact of the radiation-induced effects on their performance and reliability [24, 25]. A specialized SHMS shield house design was thus developed at Jefferson Lab. Shielding thicknesses were optimized using a Monte Carlo simulation and benchmarked against the HMS shielding house, which has proven to provide the necessary detector shielding over more than a decade of experiments at the 6 GeV JLab. A full description of the shielding optimization can be found in Ref. [23].

The primary particle radiation is created when the

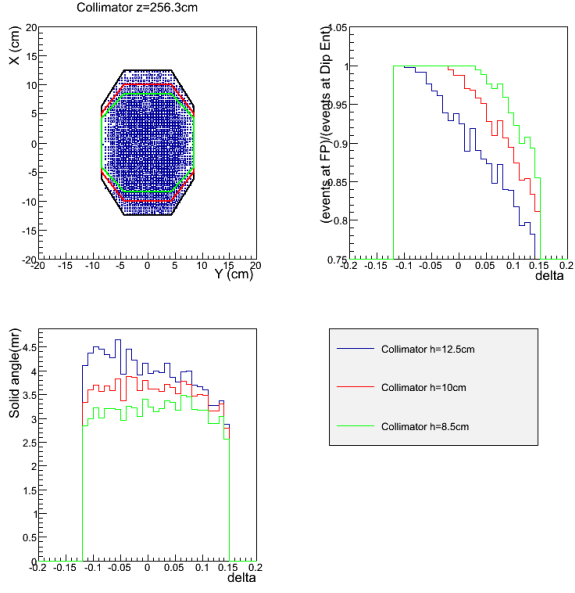


Figure 3: The upper left figure is distribution of events at the location of the collimator with three different vertical size collimators. The lower left figure is the acceptance as a function of δ for each of the collimators. The upper right figure is the fraction of events lost in the dipole bore after the dipole entrance.

CEBAF electron beam strikes the experimental target. The main components are scattered electrons, neutral particles (photons and neutrons), and charged hadrons. The energy spectrum of this radiation depends on the incident beam energy and decreases generally as $1/E$. It has been shown that the most efficient way to protect the experimental equipment from radiation damage is to build an enclosure around it using certain key materials. The type and thickness of the shield house walls depends on the energy and particle one needs to shield against. However, one may qualitatively expect that the largest amount of shielding material is needed on the side facing the primary source, which in the case of the Hall C focusing spectrometers is the front face. Additional sources of radiation are the beampipe, which extends from the experimental target to the beam dump, and the beam dump area itself. Thus, the faces of the spectrometer exposed to direct sources of radiation are the front, beam side, and the back walls.

Primary and scattered electrons lose a significant

amount of energy as they traverse a material by producing a large number of lower energy photons through bremsstrahlung [26]. It is thus important to consider shielding materials that efficiently stop the latter as well.

Neutral particles have a higher penetration power than charged particles. They are attenuated in intensity as they traverse matter, but do not continuously lose energy. Photons interact in materials almost exclusively with electrons surrounding the atom or by pair production in the field of the nucleus. The probability for an interaction depends on the atomic number of the material. Neutrons interact with atomic nuclei in a more complicated way.

An additional source of radiation is due to charged hadrons (e.g. protons, pions). However, the probability for producing hadron radiation is relatively low, and thus will be neglected here. The shielding is, nevertheless, effective for charged hadrons. The front wall will, for instance, stop 1 GeV protons.

Fig. 5 shows a schematic of the SHMS shielding plan.

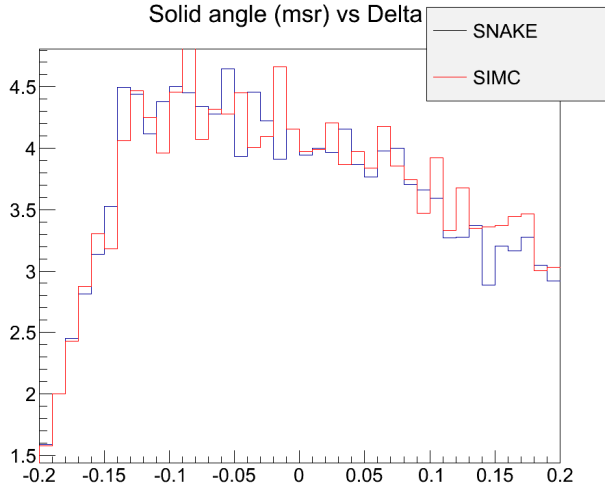


Figure 4: Comparison of predicted SHMS acceptance using the Hall C Monte Carlo (SIMC) and the magnetic transport code SNAKE.

The SHMS shield house is similar to the HMS design, but has several new features due to additional requirements. For example, the space between the beam side shield wall and the beam pipe is limited at very forward angles, and in addition, the length of the SHMS detector stack and minimum distance between the back of the detector house to the hall wall requires a reduction in thickness of the concrete shield wall.

Typical beam-target geometries were simulated using Monte Carlo techniques. Simulations were performed using the GEANT MCWORKS distribution, which includes detailed physical and geometric descriptions of the experimental hall and simulates the physics processes using standard GEANT3 together with the DINREG nuclear fragmentation package. Hadronic interactions are treated using the DINREG package, which calculates the probability of such interactions using a database of photonuclear cross sections. For electron-nucleus interactions an “equivalent photon” representation of the electron (or positron) is used.

In this simulation, the CEBAF beam electrons start 1 m upstream of the target, strike it head-on along the cylindrical symmetry axis, and have no momentum component transverse to the beamline. The simulation also includes the beam pipe, target entrance and exit windows, and the entire geometry of Hall C, including all elements of the beam dump. The transmission of

particles through the shielding materials was calculated as a function of the material thickness and the angle relative to the beam direction.

A limitation of the radiation studies is the lack of cross section data for low-energy neutrons. The accuracy of the GEANT simulations was tested by benchmark calculations using the MCNP code [27] with an isotropic neutron point source of 1 MeV located 1 m from the shield wall. The MCNP calculations suggest that 50cm of concrete thermalizes most of the fast neutrons, and after 1 m practically no epithermal neutrons remain. The thermalized neutrons can be captured by a 1cm Boron layer. In reality, however, the neutron spectrum also includes higher energy neutrons, for instance produced by electrons interacting in the concrete, and thus the actual amount of material for the walls exposed to the primary sources of radiation has to be thicker. A simple transmission calculation using GEANT4 for incident neutron beams of energies between 1 and 10 MeV suggests that a thickness 150cm of concrete is sufficient to stop the majority of low-energy neutrons [28].

The SHMS shielding model is composed of standard concrete ($\rho=2.4 \text{ g/cm}^{-3}$). The thickness of the wall in front of the detector and electronics rooms is 200 cm to shield from the primary radiation source around the target. Figure 6 shows the surviving background flux for varying front wall concrete thicknesses. The results

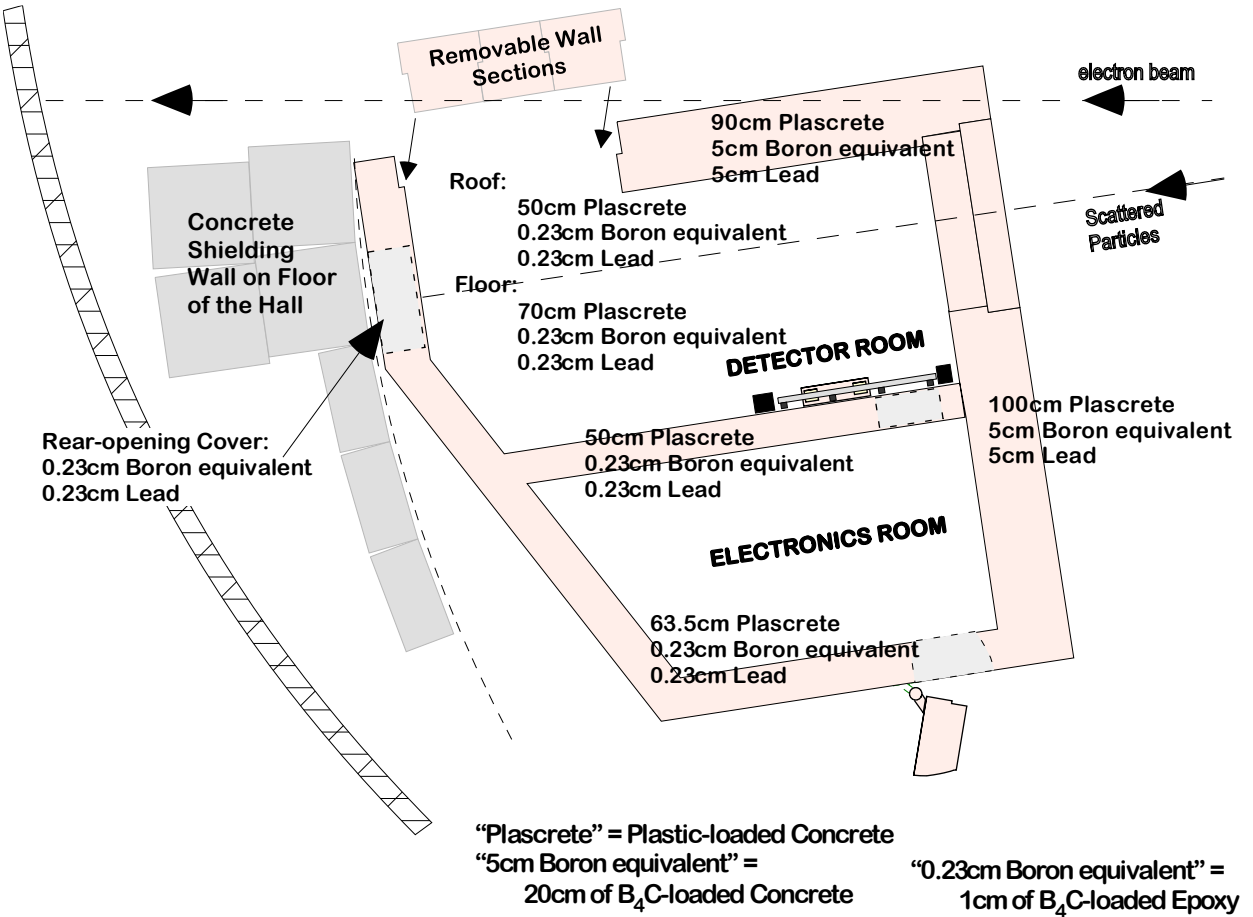


Figure 5: Plan View of the SHMS Shield House showing the layout, thickness, and composition of the walls.

are normalized to the background flux in the HMS at 20°. This angle was chosen as experiments in Hall C have shown that electronics problems seem to dominate at lower angles [29]. The simulation results suggest that 200 cm of concrete reduces the total flux to half of the HMS at 20°.

Figure 7 shows the energy spectra for surviving photons and neutrons with varying front wall thickness. In order to optimize the shielding, these secondary particles have to be absorbed as well. Our assumption on radiation damage is that photons below 100 keV will not be a significant source of dislocations in the lattice of the electronics components, while neutrons will cause radiation damage down to thermal energies. Adding lead to the concrete wall reduces the photon flux significantly, but it does not help for neutrons. On the other hand, the boron reduces the flux of very low energy neutrons. Assuming that low energy photons and neutrons cause a significant fraction of the radiation damage, then adding

the relevant material would be important.

The thickness of the beam-side wall (shielding from an extended source, the beamline) is constrained by the clearance with the detector stack inside the enclosure and the beamline at small angles. Conservatively assuming a clearance of 5cm between detector stack and the shield wall, the total concrete wall thickness is limited to 105cm. A 90cm concrete wall combined with a 5cm boron and 5cm lead layer provides the optimal shielding configuration. Adding boron is not much different from adding (or replacing) concrete, but in addition it captures thermal neutrons.

The majority of charged particles is stopped by the outer walls of the spectrometer shield house. An additional source of radiation may be created from particles entering the enclosure through the magnets. In order to protect the electronics further, an intermediate wall was installed between the detector and electronics rooms. Figure 8 shows the normalized rate as the thick-

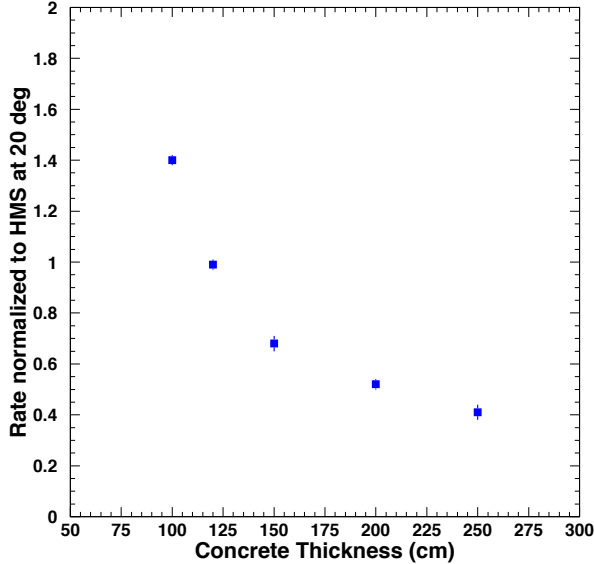


Figure 6: The normalized background rate vs. front wall thickness. The rates are normalized to those found in the HMS at 20° .

ness of this intermediate wall is varied. This suggests that the optimal configuration is provided by a concrete thickness of 80-100 cm¹. Further details on shielding configurations investigated and their optimization can be found in Ref. [23].

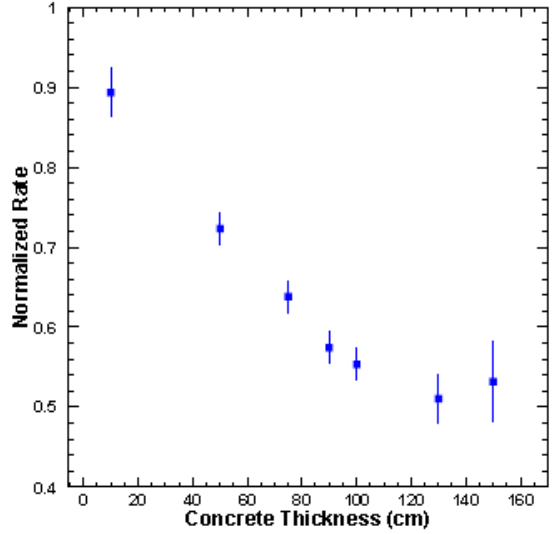


Figure 8: The normalized rate versus the intermediate concrete wall thickness.

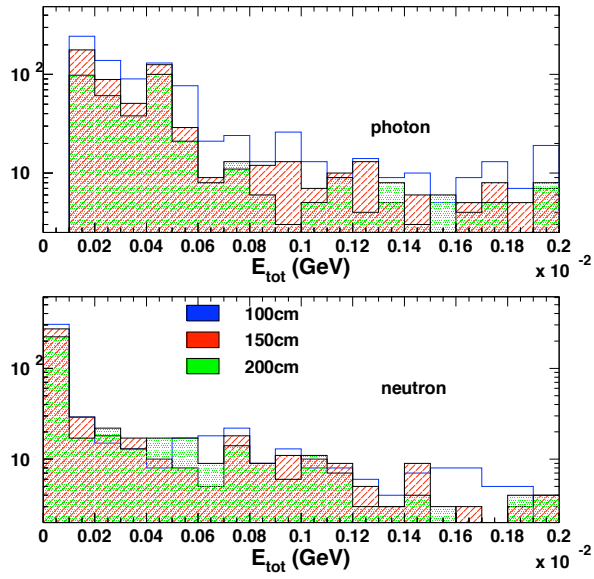


Figure 7: The outgoing particle spectrum, which is soft (< 10 MeV).

The hydrogen-rich concrete walls function as a shield, an absorber, and a neutron moderator, and are thus placed on the outside of all faces of the shield house. On the other hand, the ordering of lead and boron to shield against the photon and neutron flux may, at first glance, not be obvious, and is discussed in detail below.

The incoming photon flux has two components: externally produced photons and bremsstrahlung photons produced by electrons in the twenty radiation lengths of concrete. The simulations have shown that the outgoing photon spectrum is soft (< 10 MeV). Placing a lead layer after the concrete is essential to suppress this low energy photon flux. The (γ, n) reaction in lead is not a problem. The threshold for the reaction is given by the neutron binding energy (~ 8 MeV). At higher energies, the cross sections are in the mbarn range [30]. Even disregarding the low cross section, however, it is not clear that this reaction adds to the radiating of the electronics, because a high energy photon is replaced by a low energy (but not thermal) neutron.

¹Note that a minimum wall thickness of 50cm is needed to provide support for the roof of the shield house

425 The incoming neutron flux also has two components.
 426 Neutrons from excited nuclei will typically not exceed
 427 10 MeV. The other neutrons are produced through direct
 428 interactions with only one nucleon in the nucleus.
 429 These will have high energies, but the flux is low. As
 430 shown by the MCNP calculation, which has reliable low
 431 energy neutron cross sections, 0.5m of concrete almost
 432 fully thermalizes 1 MeV neutrons. Thus, 2m of concrete
 433 should be sufficient to thermalize the first component.
 434 Some of these will be captured in the concrete, but to eliminate the surviving thermal neutrons
 435 a layer of boron is needed. There are two relevant reaction
 436 channels: (n, γ) and $(n, \alpha\gamma)$. The former produces
 437 high energy photons, but the cross section is relatively
 438 small. The latter produces a 0.48 MeV photon for every
 439 captured neutron. The thermal cross section is about
 440 10kbarn, and even at 1 MeV it is still in the barn range.
 441 The majority of neutrons can thus be expected to be captured
 442 in a sufficiently thick boron layer. An optimal shielding
 443 configuration would also stop these photons produced in the capture. At 0.48 MeV, the photoelectric
 444 effect and Compton scattering contribute about equally
 445 to the attenuation in lead. Photons from the latter will
 446 also need to be absorbed.
 447

448 Thus, placing the lead in front of the boron layer has
 449 limited benefit. It will not affect the neutron flux, but
 450 will create an additional source of photons. The more
 451 lead one places after the boron, the more efficiently
 452 these photons will be suppressed. From the point of
 453 view of stopping bremsstrahlung photons, the order of
 454 boron and lead layers does not matter. Thus, all lead
 455 should be placed after the boron.
 456

457 Fig. 9 is a photograph showing the resulting multi-layered shielding in one of the SHMS shield house
 458 walls. The ceiling, floor, and other walls have similar
 459 compositions but varying dimensions as shown
 460 in Fig. 5. Details about the development of custom
 461 concrete material containing boron can be found in
 462 Ref. [31].
 463

464 In summary, the SHMS shielding consists of concrete
 465 walls to moderate and attenuate particles. Low energy
 466 (thermal) neutrons are absorbed in a boron layer inside
 467 the concrete. Low energy and 0.5 MeV capture photons
 468 are absorbed in lead. With this design, the rates at forward
 469 angles of 5.5° are estimated to be less than 70% of the
 470 design goal (HMS at 20°) in the detector room and below
 471 50% in the electronics room.
 472

3.3. Scintillator Trigger Hodoscopes

473 [Scintillator Hodoscopes section.](#) [Author Organizers:](#)
 474 I. Niculescu, G. Niculescu
 475

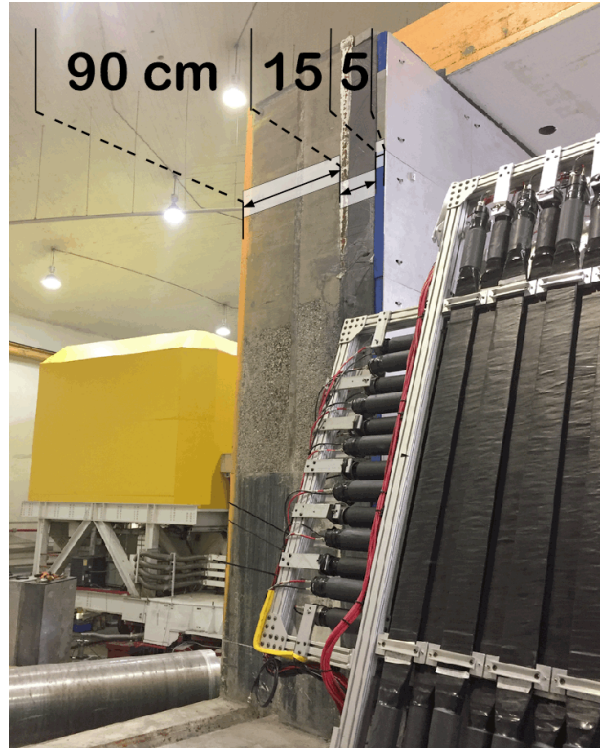


Figure 9: Photograph of the SHMS beam-side Shield Wall in cross-section view, showing the layers of different materials making up the wall.

475 The SHMS hodoscope system provides a clean trigger
 476 and trigger time information as well as the defi-
 477 nition of the detector package fiducial area, required
 478 for physics cross section measurements. The system is
 479 composed of four separate planes of detector paddles:
 480 S1X and S1Y located immediately after the second drift
 481 chamber and S2X and S2Y approximately 2.6 m away
 482 along the z direction. The S1X, S1Y, and S2X planes
 483 were built using thin scintillator paddles while S2Y uses
 484 quartz bars.
 485

3.3.1. Design and Construction

486 The overall dimensions and granularity of the three
 487 scintillator planes were driven by the Monte Carlo sim-
 488 ulations of the SHMS acceptance. The S1X and S1Y
 489 planes cover a 1000x980 mm² area while the S2X plane
 490 covers 1100x1335 mm². Further design constraints
 491 for this detector include high ($\geq 99\%$) detection effi-
 492 ciency, position independent along the scintillator pad-
 493 dle; good time resolution (~ 100 ps); high rate capabili-
 494 ty (~ 1 MHz/cm). As the detector's lifetime is assumed
 495 to be a decade or more stable, cost effective, and readily

496 available materials and readout chain were used.

497 To meet the requirements listed above the SHMS Hodo-
498 scope was built as a series of arrays (planes) of plastic
499 scintillator paddles. The S1X and S1Y planes have 13
500 1000x80 mm paddles each, while the S2X plane has 14
501 1100x100 mm paddles. For each of the three scintillator
502 planes the paddles were staggered by 7 mm and over-
503 lapped by 5 mm. To minimize the impact of the scin-
504 tillators on downstream detectors and also to ensure good
505 timing resolution the thickness of paddles was 5 mm.

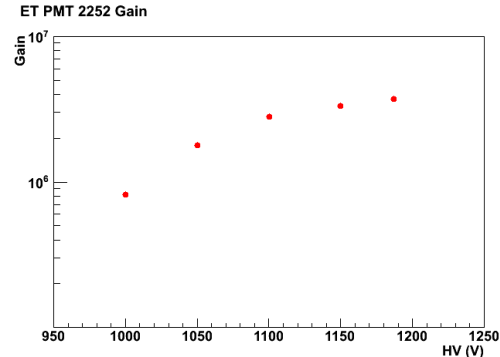
506 The scintillator material used was RP-408 ((507 <http://www.rexon.com/RP408.htm> - MAYBE add as
508 reference). The paddles were wrapped by the manufac-
509 turer with millipore paper, aluminum foil, and 2" elec-
510 trical tape. The transition between the thin scintillator
511 material and the photomultiplier (PMT) tubes used for
512 readout was done using a Lucite fishtail-shaped light
513 guide. As the glued joint between the scintillator paddle
514 and the light guide is rather fragile (5x80 and 5x100 mm
515 joints) aluminum "splints" were used to reinforce it.
516 The PMT to fishtail joint was originally wrapped with
517 2" tape as well and light-leak tested; subsequently this
518 wrapping was reinforced with TEFLON tape and a 3"
519 heat-shrink sleeve.

520 Each scintillator is read at both ends by PMTs glued
521 to the fishtail using optical glue (BC-600) matching the
522 index of refraction of the Lucite. A combination of Pho-
523 tonis XP 2262 and ET 9214B 2" tubes were used. Both
524 models have 12-stage amplification and their maximum
525 photocathode sensitivity is in the blue-green range. The
526 typical gain is 3×10^7 . Gains were measured as a func-
527 tion of high voltage during the construction and the
528 whole hodoscope was gain-matched *in situ* once in-
529 stalled in SHMS.

530 3.3.2. Performance

531 All scintillator paddles and the PMTs used to build
532 the S1X, S1Y, and S2X planes were extensively tested
533 during assembly: the dark current and the gain as a
534 function of the high voltage were measured for each
535 tube; the finished paddles were light-leak tested and
536 their detection efficiency as a function of position along
537 the paddle was measured using cosmic rays on an au-
538 tomated test stand. A typical gain versus HV graph is
539 shown in Fig. 10.

540 Once installed in the SHMS detector hut all pad-
541 dles were retested and gain-matched. During the Hall
542 C commissioning experiments carried out during the
543 Spring 2018 the scintillators performed as expected
544 with no major problems. Might want to put more text/a
545 picture here, maybe time resolution, efficiency, etc?



546 Figure 10: Gain versus high voltage graph for an ET
547 tube used for the scintillator hodoscope.

548 3.4. Quartz-bar Trigger Hodoscope

549 Quartz Hodoscope section. Author Organizer: S. 550 Malace

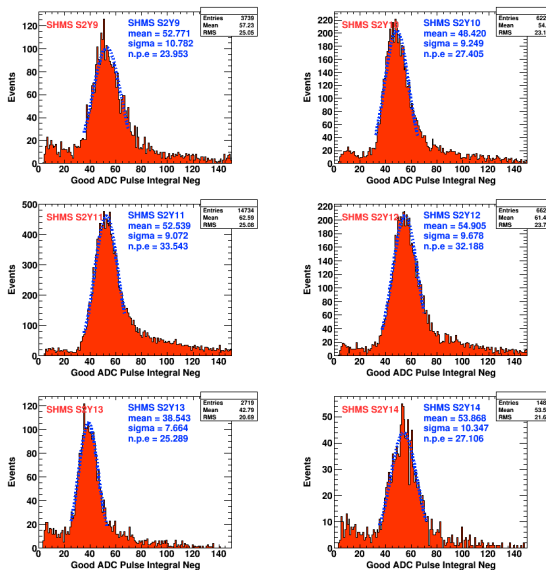
551 The SHMS hodoscope quartz plane was designed to
552 help with neutral background rejection in the 12 GeV
553 high-rate environment. It operates on the principle of
554 Cherenkov light production by electrically charged par-
555 ticles. It is one of the four hodoscope planes that form
556 the basic 3 out of 4 trigger in the SHMS. In what fol-
557 lows the design and construction of this detector will be
558 presented as well as its performance with electron beam
559 in Hall C.

560 3.4.1. Design and Construction

561 The design and construction of the SHMS ho-
562 doscope quartz plane was done by the North Car-
563 olina A&T group led by Abdellah Ahmidouch and
564 Samuel Danagoulian. Quartz bars of x,y,z dimen-
565 sions with an index of refraction of 1.5 were chosen. The
566 Cherenkov light produced by electrically charged par-
567 ticles was detected by quartz window ET9814QB pho-
568 tomultiplier tubes optically coupled to the quartz bars
569 through RTV615 rubber silicon of 50μ thickness. Af-
570 ter a while in storage the quartz window photomulti-
571 plier tubes showed signs of vacuum contamination (He
572 gas poisoning was suspected) and were eventually re-
573 placed at Jefferson Lab with UV-glass window PMTs
574 ET9814WB. There are 16 bars in use in the hodoscope
575 quartz plane with an overlap between adjacent bars of
576 x cm. This covers x % of the SHMS acceptance. The
577 quartz plane frame allows for more bars to be added.

576 **3.4.2. Performance**

577 The performance of the detector was studied with
 578 beam during the Hall C commissioning in Fall of 2017.
 579 A plot of the photoelectron response from most bars in
 580 the quartz plane is shown in Fig. 11 and Fig. 12. Only
 581 electrons with an incident angle close to 90 deg were
 582 chosen here to eliminate the bias coming from possibly
 583 reduced photon collection efficiency due to sub-optimal
 584 angles of the photon cones. All PMTs and optical cou-
 585 plings performed satisfactory.

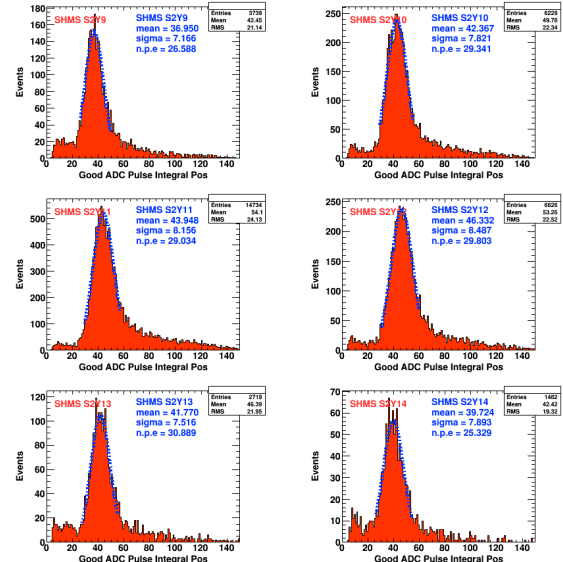


586 Figure 11: Number of photoelectrons response from the
 587 quartz plane.

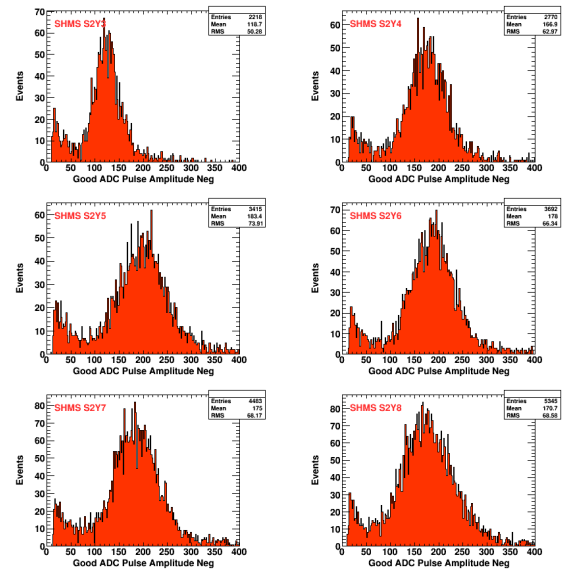
588 The threshold for Cherenkov light production in the
 589 quartz bars for electrons, pions, kaons and protons is
 590 shown in Fig. bla. Beam data confirmed the expectation
 591 that the detection efficiency for low momnetum protons,
 592 for example, will be smaller than that for pions or elec-
 593 trons simply due to the reduced number of Cherenkov
 594 photons that particles close to their firing threshold will
 595 produce. This is exemplified by Fig. 13, Fig. 14 and Fig.
 596 15.

597 **3.5. Drift Chambers**

598 The SHMS horizontal drift chambers provide infor-
 599 mation to determine the trajectory of charged particles
 600 passing through the detector stack. The drift chamber
 601 package consists of two horizontal drift chambers sepa-
 602 rated by a distance of 1.1 m and oriented in the detector
 603 stack such that the sense wires planes are perpendicular
 604 to the central ray. Each chamber consists of a stack of
 605 six wire planes providing information on the track position
 606 along a single dimension in the plane of the wires
 607 and perpendicular to the wire orientations to better than
 608 $250 \mu\text{m}$. The perpendicular distance of the track relative
 609 to the wire is determined from the time of the signal
 610 produced by the ionization electrons as they drift from



586 Figure 12: Number of photoelectrons response from the
 587 quartz plane.



586 Figure 13: PMT pulse amplitude from pions with
 587 momenta of 1.96 GeV.

588 six wire planes providing information on the track position
 589 along a single dimension in the plane of the wires
 590 and perpendicular to the wire orientations to better than
 591 $250 \mu\text{m}$. The perpendicular distance of the track relative
 592 to the wire is determined from the time of the signal
 593 produced by the ionization electrons as they drift from

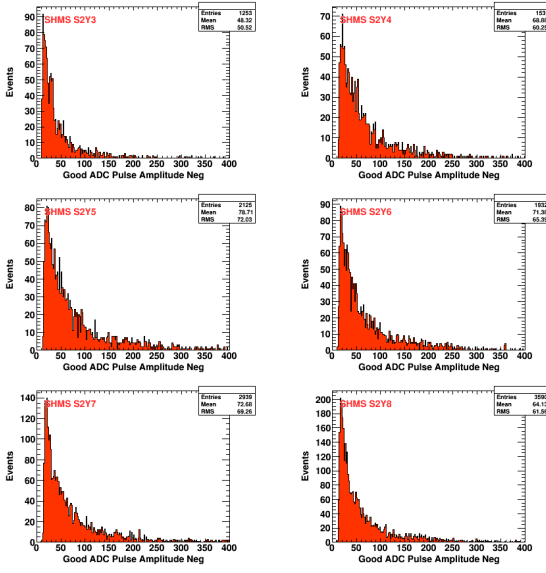


Figure 14: PMT pulse amplitude from pions with momenta of 1.96 GeV.

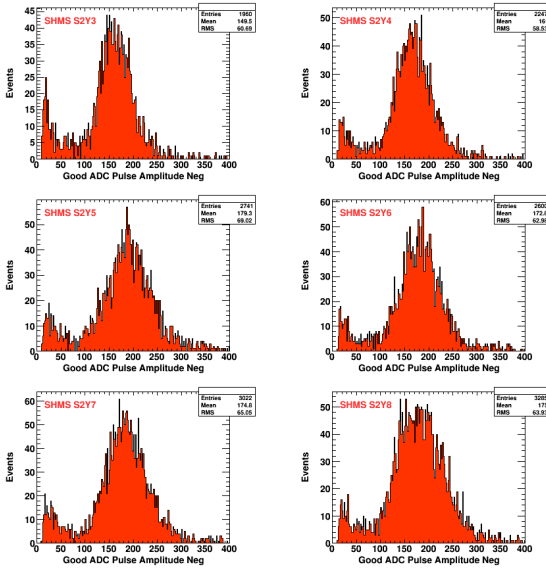


Figure 15: PMT pulse amplitude from protons with momenta of 5.05 GeV.

their production point to the wire in an electric field of approximately 3700 V/cm.

The basic design and construction technique is based on that of previous successful chambers built for the Hall C 6 GeV program, which have been shown to reach the resolutions and particle rate specifications

of the SHMS. The open layout design consists of a stack of alternating wire and cathode foil planes; each plane consisting of 1/8 inch thick printed circuit board (PCB). These are sandwiched between a pair of aluminum plates on the outside, which provide both the overall structural support and the precise alignment of each board via dowel pins at the corners. Just inside each plates is a fiberglass board with the central area cut out and covered with a vacuum stretched film of aluminized Mylar, which provides the gas window. These are sealed to prevent gas leakage via an o-ring around the gas fitting through-hole on the inside of the plate.

Each chamber consists of two identical half chambers separated by a fiberglass mid-plane, which is utilized for mounting the amplifier discriminator cards required for the sense wire readout. To minimize the production costs, only two unique PCB types were designed: an X-plane with wires oriented horizontally (Left Panel of Figure 16), and a U-plane with wires oriented at +60 degrees relative the X-plane (Right Panel of Figure 16). All other plane orientations are generated by rotations of these two basic board types. For instance, the boards are designed such that a rotation of 180 in-plane about an axis through the center of the board produces boards with wires of the same orientation, but shifted by 1/2 cell width, thus allowing the resolution of left/right ambiguities. Rotation of Figure 16 such that the top becomes the bottom produces the X' and U' orientations. The V and V' boards with wire orientation of -60 degrees relative to the X-plane are produced by a rotation of the U and U' boards of 180 degrees into the page about a vertical axis though the center of the board. Each half chamber has three planes with the first half consisting of (U, U', X) and the second half consisting of (X', V', V). The first chamber is oriented in the SHMS frame such that the board ordering as seen by particle transversing the spectrometer is (U, U', X, X', V', V), while for the second chamber the ordering is reversed (V, V', X', X, U', U). A drawing showing the chambers mounted in the frame is presented in Figure 17.

The drift gas (50/50 mixture of Ethane/Argon in production mode) flows across each board through holes in the cathode planes (k-planes) alternating from top to bottom. A technical drawing of a k-plane is presented in Figure ???. The overall dimensions of the wire chambers are driven by the desired active area for particles at the focal plane of the SHMS; this has been set at 80 cm x 80 cm. The active area of each wire plane consists of alternating 20 μ m diameter gold tungsten sense wires and 80 μ m diameter copper plated beryllium field wires separated by 0.5 cm. Each wire plane is sandwiched be-

667 between a pair of cathode planes with the cathode surfaces 694
668 consisting of 5 mil thick stretched foils of copper plated 695
669 Kapton. 696

670 3.6. Heavy-Gas Čerenkov Counter 697

671 Heavy-Gas Čerenkov Counter section. Author Orga- 698
672 nizer: G. Huber, w/R. Ambrose 700

673 3.6.1. Design 701

674 The SHMS Heavy-Gas Čerenkov detector (HGC) is 702
675 a threshold-type Čerenkov detector, designed to sepa- 703
676 rate charged π and K over most of the SHMS operating 704
677 momentum range, 3–11 GeV/c. C_4F_8O radiator gas at 705
678 1 atm, with an index of refraction of $n=1.00137$ at stan- 706
679 dard temperature [14], allow π^\pm to produce abundant 707
680 Čerenkov light above 3 GeV/c momentum, while K^\pm 708
681 remain below Čerenkov threshold until about 7 GeV/c. 709
682 Optimal π/K separation at higher momenta require 710
683 a reduction in the gas pressure, down to 0.3 atm at 711
684 11 GeV/c. 712

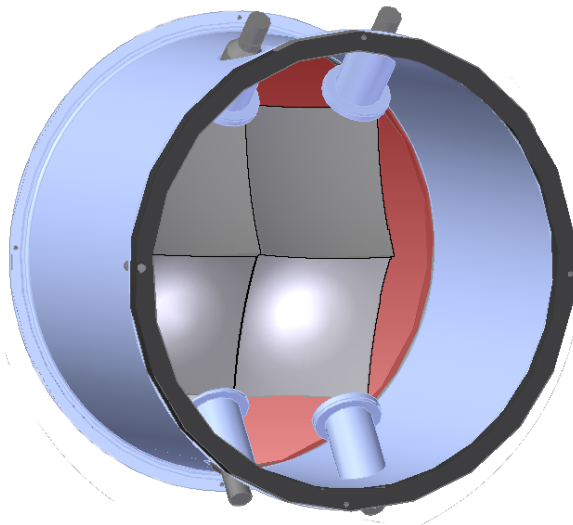


Figure 18: 3D-CAD rendering of the Heavy Gas Čerenkov Detector.

685 A schematic view of the detector is shown in Fig. 18. 736
686 The SHMS focal plane is subtended by four 55×60 cm 737
687 0.3 cm thick glass mirrors, which reflect the Čerenkov 738
688 radiation to four Hamamatsu R1584 12.5 cm photomul- 739
689 tiplier tubes located above and below the particle en- 740
690 velope. The mirrors and gas are enclosed in a cylin- 741
691 drical aluminum tank of 164.9 cm inner diameter and 742
692 113.5 cm length, with entrance and exit windows of 743
693 0.102 cm thickness 2024 T-4 aluminum alloy [15]. The 744

vessel is sufficiently strong to be pumped to vacuum before introducing the radiator gas, avoiding the need to purge when filling. A unique aspect of the detector is the placement of the photomultipliers outside the gas envelope, viewing the enclosure through 1.00 cm thick Corning 7980 quartz windows. This allows the gas enclosure to be smaller in diameter than otherwise, as the full length of the PMT and base no longer had to be fully within the diameter of the vessel. It also makes the PMTs available for servicing without venting the gas.

The mirrors are inexpensive, having been produced by the slumping process [16]. As a result, they deviate from the desired 110 cm radius of curvature with a slightly oblate shape [17]. However, the Čerenkov cone on the mirrors for 3–7 GeV/c π^\pm in C_4F_8O is 7–10 cm in diameter, so optical quality mirrors are not required for this application. The UV wavelength characteristics of the respective optical components are relatively well matched. C_4F_8O has a good transmittance down to ~160 nm [14]. The quartz viewing windows provide >88% transmission down to 200 nm, including the ~10% loss due to surface reflection [18], and the optical glass face PMTs have 70% of their peak quantum efficiency at 200 nm (peak at 350 nm) [19]. Accordingly, the mirror reflectivity was optimized for >90% at 270 nm, and 75% at 200 nm [20].

720 3.6.2. Calibration

721 The goal of the calibration procedure is to generate a 722 reliable translation from raw fADC channels (or charge 723 in pC) to the physically meaningful number of photo- 724 electrons (NPE), that is, the number of electrons emitted 725 from the cathode surface of the PMT. This is achieved 726 by isolating the single photoelectron (SPE), yielding a 727 calibration, and then verified by examining the linear 728 spacing of the first few photoelectrons and that the NPE 729 populations of each PMT follow Poisson statistics.

730 To reveal the SPE, tracking cuts are applied to the 731 data to analyze what each PMT detected from charged 732 particles traversing each mirror quadrant. As a charged 733 particle passes through a mirror quadrant, the base of 734 the produced Čerenkov cone will allow some light to 735 be incident on adjacent mirrors. As each mirror is 736 focused on a single PMT, one PMT will receive most of 737 the produced light while the other three receive much 738 smaller amounts. This small signal allows the SPE to 739 be measured, thus giving the calibration. For example, 740 if an e^- passes through the top left mirror of Figure 18, 741 a large amount of light is received by the top left PMT. 742 Since so much light is received by the PMT, a large 743 number of photoelectrons will be produced, making it 744 difficult to resolve the SPE. However, due to the spread

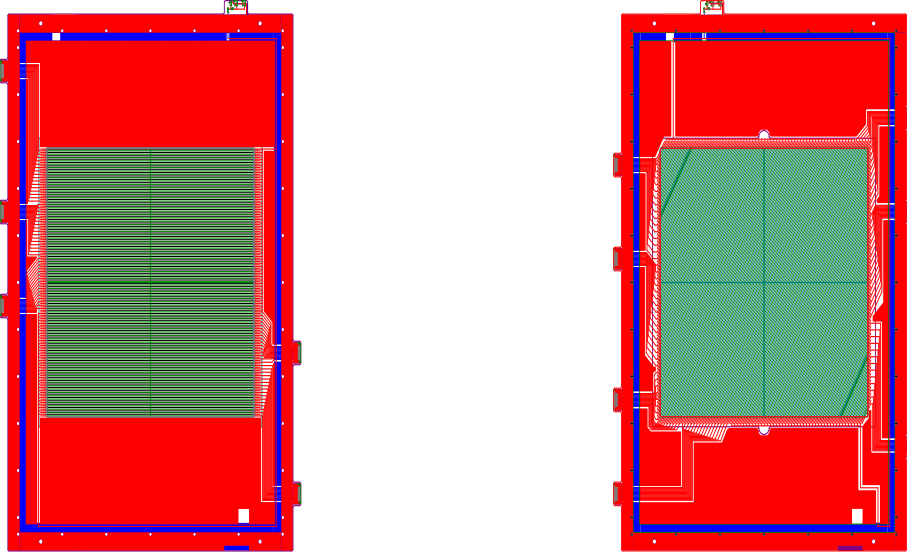


Figure 16: Technical drawings of the PCBs for the X-plane (Left) and U-plane (Right).

of the Čerenkov cone, very little light will be incident on the two adjacent mirrors, the top right and bottom left. Those two mirrors in turn reflect very little light onto the top right and bottom left PMTs. A small number of incident photons means only a few photoelectrons will be produced, revealing the SPE for those two PMTs.

Several cuts are applied to the data to perform this analysis. A tracking cut is required, given by

$$x_{\text{HGC}} = x_{\text{Focal Plane}} + x'_{\text{Focal Plane}} * z_{\text{HGC}}, \quad (2)$$

$$z_{\text{HGC}} = 156.27 \text{ cm}, \quad (3)$$

to give the location of events in the HGC mirror plane. The coordinate axis for the HGC is the convention used in charged particle transport in dispersive magnetic systems. The x -axis is the direction of increasing particle momentum, the z -axis is the direction of particle travel through the spectrometer, and the y -axis is deduced from $z \times x$. The focal plane parameters are obtained from the tracking algorithm, and an identical formula gives the distribution of events in the y -axis. The selection for the (x, y) tracking cut is defined on the physical dimension of the mirror quadrants. A timing cut is applied to the HGC data, collected using the high resolution pulse time setting in the FADC250's FPGA. The time measured corresponds to the time it takes a pulse to reach half of its maximum amplitude after passing a pedestal threshold of 5 mV. Lastly, a cut on particle velocity, β , is also applied, again obtained from the tracking algorithm.

An example of a completed calibration is shown in Figure 19. Illustrated is the isolated SPE, along with the second and third peaks to demonstrate linearity. In this figure, the calibration constant has already been applied to the data, yielding a distribution in units of NPE. To verify the linear spacing of the peaks, the spectrum is fit with a sum of three Gaussian distributions shown by the red line. The fit results are shown on the inset box, where the means of the Gaussian fits are consistent with the photoelectron peaks. Figure 20 is from the same calibration, displaying that the calibrated PMT population follows the expected Poisson statistics. PMT 1 is shown, where particle identification criteria is applied to obtain a Poisson distribution. Namely, e^- were selected by placing a cut on the calorimeter's normalized energy. For this run, the HGC was filled with CO₂ at 1 atm, corresponding to a π momentum threshold of 4.65 GeV/c², at a central momentum in the SHMS of -3.0 GeV/c². Since the momentum of produced π will be so far below threshold, a very clean sample of e^- can be selected.

An inherent systematic uncertainty is present in the HGC calibration due to statistical fluctuations in determining the location of the SPE in the various mirror quadrants. This uncertainty was quantified by recording the locations of the SPE across several runs, across each mirror quadrant, for each PMT. The systematic uncertainty in the calibration is taken to be the root mean square of this set of values, giving 1.8%. It should be

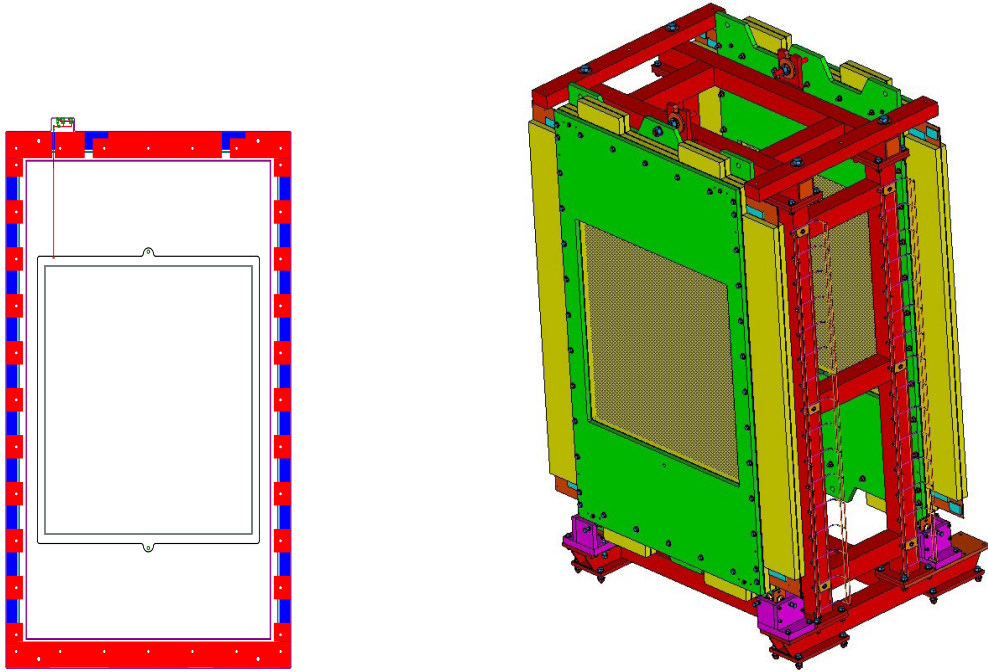


Figure 17: (Left) Technical drawing of cathode (k-plane) PCB. (Right) Technical drawing of the two drift chambers mounted in the Aluminum frame such that the scattered particles would enter the chamber from the left. The chambers are fixed to the frame by a bolt through the top tab on the chamber plate which allows for fine adjustments to the pitch. The downstream chamber (DC2) is mounted in the reverse orientation from the upstream chamber (DC1).

noted this uncertainty is a factor of three larger than the statistical uncertainty of the SPE peak, which is 0.6%.

3.6.3. Gain Matching

To ensure each PMT has an identical response to incident light, the voltages of each PMT were adjusted to obtain accurate gain matching. This can be seen in Figure 21 by the alignment of the SPE at approximately 6.825 pC, represented by the band across all four PMTs. Additionally, the gain of each PMT was tested by the manufacturer, Hamamatsu, and at Jefferson Lab. The results of each test are shown in Table 3. The Hamamatsu data were taken directly at 2000 V in a highly controlled environment, thus leading to small uncertainty in the gain which was not quoted. The Jefferson Lab measurement were also taken at 2000 V, but taken in an experimental environment. This gives rise to an uncertainty in the JLab gain data on the order of 1%, larger than the Hamamatsu data.

3.6.4. Performance

The performance of the HGC is determined by the capacity to separate particle species on the basis of

produced NPE. In particular, the HGC is a threshold Čerenkov detector and thus identifies species based on whether or not a signal greater than 1.5 NPE was generated or not. The first metrics of performance to be discussed are the detector efficiency and contamination.

Efficiency in this context refers to the ratio of events selected as a particular particle species by all detectors in the SHMS, including the HGC, over the number of events selected as that same species without any information from the HGC. This is illustrated by the equation

$$\eta_{\text{HGC}} = \frac{e^- \text{ detected with HGC signal}}{e^- \text{ detected without HGC signal}}, \quad (4)$$

where η_{HGC} represents the detector efficiency of the HGC and an e^- is used for example. The selection criteria includes cuts on the calorimeter's normalized energy, beta reconstruction, timing information, and a single reconstructed track. Contamination refers to the number of events identified as a sub-threshold particle by the calorimeter and aerogel Čerenkov, but produced more than 1.5 NPE in the HGC. For example, if the HGC is configured for e^-/π^- separation, the π^- contamination is

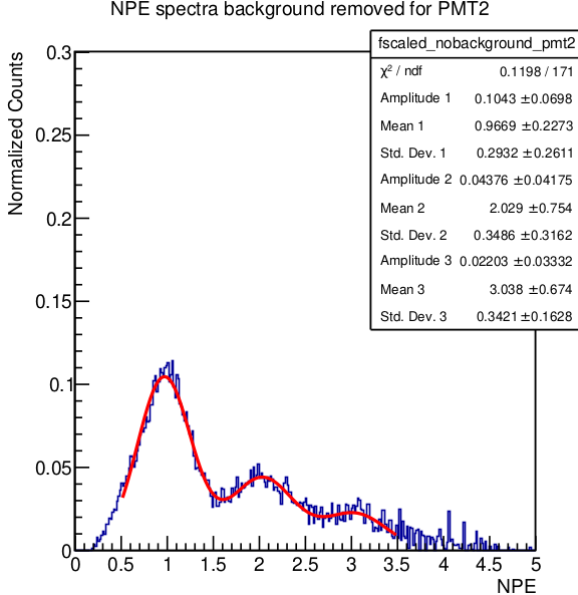


Figure 19: Results from a successful calibration of the HGC. Shown is the isolated single photoelectron peak and the linear spacing of the first three photoelectron peaks. The red fit is a sum of three Gaussian distributions to verify the spacing of the photoelectron peaks.

835 defined as the number of events identified as a π^- by all
836 detectors, except the HGC, which identified an e^- .

PMT	JLab Gain	Hamamatsu Gain
PMT 1	$(2.79 \pm 0.01) \times 10^7$	0.969×10^7
PMT 2	$(6.55 \pm 0.04) \times 10^7$	3.60×10^7
PMT 3	$(7.12 \pm 0.05) \times 10^7$	5.79×10^7
PMT 4	$(5.35 \pm 0.04) \times 10^7$	3.20×10^7

Table 3: Gain characteristics for the PMTs in the HGC. Two measurements were performed, one at Jefferson Lab in an experimental setting, and one by the manufacturer Hamamatsu. The set voltage for the gain measurements is 2000 V for each PMT.

PID Configuration	Efficiency	Contamination
e^-/π^-	95.99%	10000 : 1
π^+/K^+	98.22%	1000 : 1

Table 4: Summary of the Heavy Gas Čerenkov performance in separating between particle species. Efficiency is based on a photoelectron cut greater than 1.5.

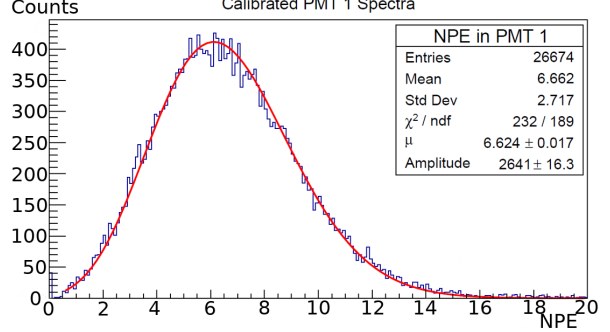


Figure 20: Results from a successful calibration of the HGC. Shown is the NPE population of PMT 1 overlayed with a red fit of a Poisson distribution.

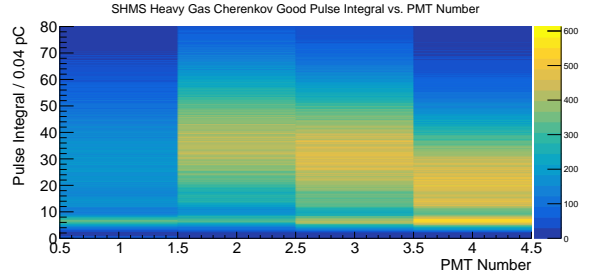


Figure 21: Demonstration of gain matching between PMTs by the alignment of the single photoelectron, indicated by the yellow band about 6.825 pC. The horizontal axis refers to PMT number, the vertical axis to Pulse Integral in bins of 0.04 pC. The color axis represents the number of events filling each bin.

837 Two runs are chosen to show HGC efficiency and
838 contamination, one where the HGC separated between
839 e^-/π and the other π/K . The former featured the HGC
840 filled with CO_2 at 1 atm and a SHMS central momen-
841 tumbus of $-3.0 \text{ GeV}/c^2$. Particle identification was estab-
842 lished by a cut on the normalized calorimeter energy. The lat-
843 ter had the HGC filled with $\text{C}_4\text{F}_8\text{O}$ at 1 atm, giving a
844 π momentum threshold of $2.8 \text{ GeV}/c^2$ and a K momen-
845 tum threshold of $9.4 \text{ GeV}/c^2$, at a SHMS central momen-
846 tum of $+5.05 \text{ GeV}/c^2$. Particle identification was
847 performed by a cut on the aerogel Čerenkov detector
848 and the normalized calorimeter energy. The spectrum
849 obtained for the π/K separation is shown in Figure 22.
850 This figure illustrates the broad distribution of NPE pro-
851 duced by π , fit with the red curve, which are above their
852 momentum threshold. At the lower end of the NPE
853 axis, there is a very large number of events producing
854 no light, or just the SPE. These events correspond to K

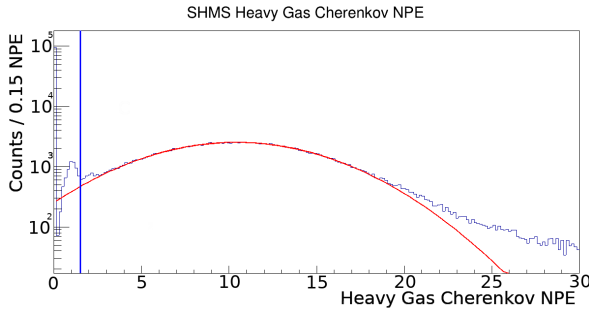


Figure 22: Demonstration of the particle identification capability of the Heavy Gas Čerenkov. Pictured is the separation between π and K , π giving the broad distribution of NPE and fit with the red Gaussian and the K giving the large signal at 0 NPE. The prominence of the single photoelectron peak is attributed to delta-rays or knock-on e^- . The vertical blue line represents the threshold in NPE of the HGC, events above this threshold are identified as π , events below are K .

since they are below the momentum threshold to produce Čerenkov light. The presence of the SPE is likely due to δ -rays, or knock-on e^- , a phenomenon where K can ionize the Čerenkov media and produce e^- which produce Čerenkov radiation. The vertical blue line indicates the NPE threshold, above which events are identified as π , below which are K . The summary of the particle identification efficiency and contamination is shown in Table 4.

Lastly, measurements of the π efficiency across a variety of momentum settings can be used to verify the index of refraction of the Čerenkov media. The relationship between π efficiency and momentum is fit with the equation [21]

$$\eta_{HGC} = 1 - e^{-(p-p_o)/\Gamma}, \quad (5)$$

where η_{HGC} is the detector efficiency, p is the momentum of the π , and p_o and Γ are free parameters. Data taken in the range of 2.53 GeV/c to 5.05 GeV/c with the HGC filled with C_4F_8O yields an index of refraction of $n = 1.001 \pm 0.002$. This is in agreement with the accepted value of $n = 1.00139$ [22].

3.7. Noble-Gas Čerenkov Counter

[Heavy-Gas Čerenkov Counter section. Author Organizer: D. Day](#)

3.7.1. Design

Analyzing momenta up to 11 GeV/c at scattering angles from 5.5 to 40.0 degrees, the SHMS will reach

kinematic regions in which the pion background rate dominates the scattered electron rate by more than 1000:1. The suppression of these anticipated pion backgrounds while maintaining efficient identification of electrons is therefore one of the main duties of the SHMS detector elements and the SHMS Noble Gas Čerenkov Detector shoulders a large portion of this particle identification burden. The design of the noble gas threshold Čerenkov detector is such that it will meet these twin goals of suppression and identification. The main goal of the detector is to distinguish between electrons and pions with momenta between 6 GeV and 11 GeV/c. Operating at 1 ATM it will use a mixture of Argon and Neon as the radiator: pure Argon with an index of refraction $n=1.00028201$ at a SHMS momenta of 6 GeV/c and pure Neon with an index of refraction $n=1.000066102$ at 11 GeV/c and a mixture of Argon and Neon at intermediate momenta.

The SHMS NGC design was restricted by the available space and the need to have good discrimination at the highest momenta. The number of photoelectrons is maximized in this design by the use of quartz window PMTs and mirrors with excellent reflectivity well into the UV.

The NGC consists of the XX main elements: 1) a light tight box with thin entrance and exit windows designed to operate at 1 Atm, 2) four spherical mirrors held in a rigid frame, and 3) four 5 inch quartz window photomultipliers (PMTs) and 5) the radiator gas.

The tank was fabricated with an internal rigid aluminum t-slot frame and thin aluminum walls welded together and has an active length of 2m along the beam direction and approximately 90 cm perpendicular to the beam direction. The main access is provided through a large 'door' and four small panels provide modest access to the PMTs. The tank has feed throughs for gas management as well as for HV and signal cables. The interior was painted with a black flat paint to prevent the reflection of light from cosmic rays or hall background. Thin entrance and exit window made of two layers of 2 mils of the Dupont product, Tedlar - $(CH_2CHCl)_n$. The PMTs were positioned outside the active area of the scattered particles, achieved by a 15° tilt of the mirrors.

Four spherical thin glass mirrors of radius 135 cm, square in shape with edges of 43 cm focus the Čerenkov light onto to the PMTs. The glass blanks were manufactured by Rayotek Scientific[?] of San Diego from borosilicate glass of 3 mm thickness by slumping over a polished steel mold and then cut to dimensions. As simulation showed a reduction of collection efficiency due to incoming photons losses at the exposed edges of the mirror were beveled away from the active surface

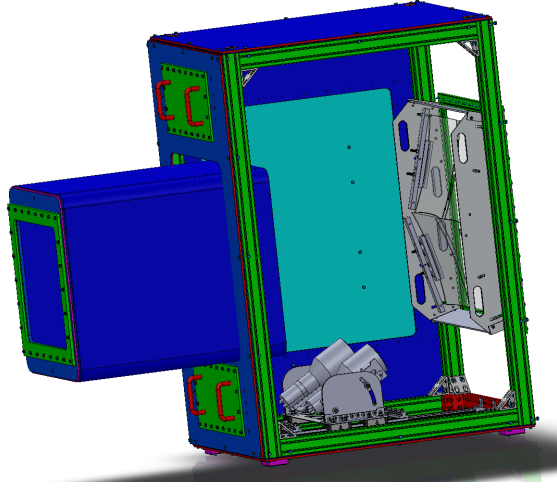


Figure 23: Sketch of the NGC tank. This view is possible as one panel is removed. Note the PMT mounting system is different than shown here.

928 to minimize scattering from these edges.

929 The final batch of the glass blanks was shipped to
 930 Apex Metrology Solutions of Fort Wayne for the CMM
 931 shape scanning measurements. Apex's measurements
 932 were performed on the grid of 1806 points. The data
 933 were fitted with spherical, conical and elliptical fit func-
 934 tions for each mirror. Though the elliptical fit de-
 935 scribed the surface slightly better than the spherical fit
 936 the updated simulation with the real measured parame-
 937 ters showed almost no difference in the collection effi-
 938 ciency between the two. In addition the same fitting was
 939 performed for 5 selected locations on the mirror: entire
 940 mirror, the center, and 4 quadrants. Based on the spheri-
 941 cal fit results "best" mirrors and "best" corners for each
 942 mirror were identified. The 4 mirrors come together and
 943 overlap at the center of the acceptance where a major-
 944 ity of the scattered electrons are focused. Care was then
 945 made to select among the best 4 glass pieces their best
 946 corners so as to be in the overlap region. The radii of the
 947 4 best pieces of glass, from fitting, was found to never
 948 vary by more than 2 cm from the contracted value of
 949 135 cm in fit areas described above.

950 Specially constructed packaging was constructed that
 951 made contact with the active surface all but impossi-
 952 ble for shipment (and return) to CERN where they were
 953 coated by the Thin Film and Glass Service of the Detec-
 954 tor Technologies Group at CERN[?]. The reflectivity
 955 was measured at CERN and found to be excellent well
 956 into the UV - See Figure 24

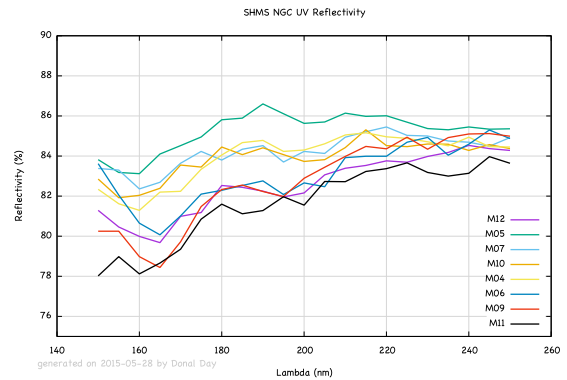


Figure 24: The UV measured reflectivity of the finished mirrors, coated at CERN which is no less than 78% at 150 nm. Between 250 nm and 600 nm the reflectivity rises to almost 90%.

957
 958
 959
 960
 961
 962
 963
 964
 The four mirrors are arranged two above two ar-
 ranged to overlap in the center, providing full coverage
 of the active area. In order to accomplish this the mir-
 rors were order at slightly different z-positions (beam
 direction). The mirrors were mounted in a monolithic
 frame installed as single unit. See Figure 25 The mir-
 rors are tilted by 15° to allow the PMTs to be outside
 the active area.



Figure 25: Frame with mirrors about to be moved into tank.

965
 966
 967
 968
 969
 The four PMTs are 14 stage 5 inch quartz window
 PMTs manufactured by Electron Tubes Enterprises [?]
 , model 9823QKB04. The tubes are surrounded by a
 mu-metal shield and the HV is distributed to the stages
 by a positive base. The 9823QKB04 has a quantum effi-
 ciency above 5% at 150 nm and 30% at 350 nm as seen

971 in Figure 26.

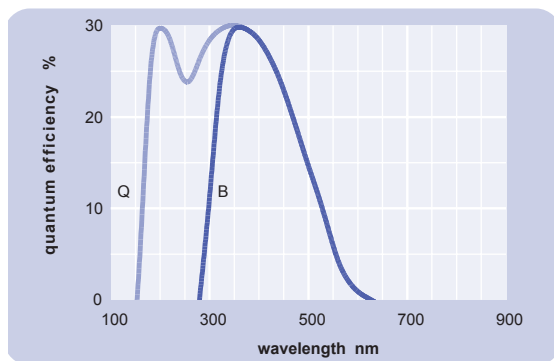


Figure 26: Quantum efficiency of Electron Tubes Enterprises model 9823QKB04 - light blue curve, labelled "Q".

- 972 3.7.2. *Optics Tuning*
- 973 3.7.3. *Calibration*
- 974 3.7.4. *Gain Matching*
- 975 3.7.5. *Performance*

976 3.8. Aerogel Čerenkov Counter

977 [Aerogel Čerenkov Counter section](#). Author Organizer:
978 T. Horn

979 Comprehensive article published in NIM A842
980 (2017) 28-47. [13].

981 3.8.1. General Design Overview

982 The detector design is summarized in Fig. 27 which
983 shows a photograph of the aerogel counter installed
984 downstream of the cylindrical HGC in the SHMS
985 detector stack. The detector consists of two main com-
986 ponents: a tray which holds the aerogel material, and a
987 light diffusion box with photomultiplier tubes (PMTs)
988 for light readout. Four identical trays for aerogel of
989 nominal refractive indices of 1.030, 1.020, 1.015 and
990 1.011 were constructed. The design allows for easy de-
991 tector assembly and replacement of the aerogel trays.
992 Using up to 9 cm aerogel thickness in the trays, the total
993 depth of the detector is 24.5 cm along the optical axis of
994 the SHMS. A detailed discussion of the detector, char-
995 acterization of its components, and performance tests
996 can be found in Ref. [32].

997 The diffusion box is made of the aluminum alloy
998 6061-T6. The side panels are constructed of ~2.5 cm
999 (1-inch) plates. The back cover is ~1.6 mm (1/16 inch)
1000 thick. The inner dimensions of the box are ~ 103 ×
1001 113 × 17.3 cm³ (40.5" × 44.5" × 6.82"). To optimize
1002 light collection the inner surface of the diffusion box is
1003 lined with either 3 mm (covering ~60% of the surface)
1004 or 1 mm (remaining ~40% of the surface) thick GORE
1005 reflector material [33]. This material has a reflectivity
1006 of about 99% over the entire spectrum.

1007 The light collection is handled by 5-inch diameter
1008 photomultiplier tubes (XP4500). The 5.56" (14.1 cm)
1009 diameter cylindrical housings holding the PMTs are
1010 mounted upon 14 waterjet cut circular openings on the
1011 left and right (long) sides of the diffusion box, with
1012 minimum spacing of 14.92 cm (5.875") between the
1013 centers. The PMTs are sealed into their housing us-
1014 ing a light-tight synthetic rubber material (Momentive
1015 RTV103 Black Silicone Sealant) and the whole assem-
1016 bly is sealed light-tight. The mechanical design includes
1017 six openings on the top of the diffusion box, presently
1018 covered with blanks, that can be used to increase the sig-
1019 nal output from the detector by about 30%, if needed.

1020 The magnetic shielding for the PMTs consists of 13.5
1021 cm (5.316") diameter μ -metal cylinders, which were
1022 constructed to end abreast with the PMT window. The
1023 construction also features bucking coils that can be in-
1024 stalled on the PMTs, if excessive residual magnetic
1025 fields appear to be present in the SHMS hut.

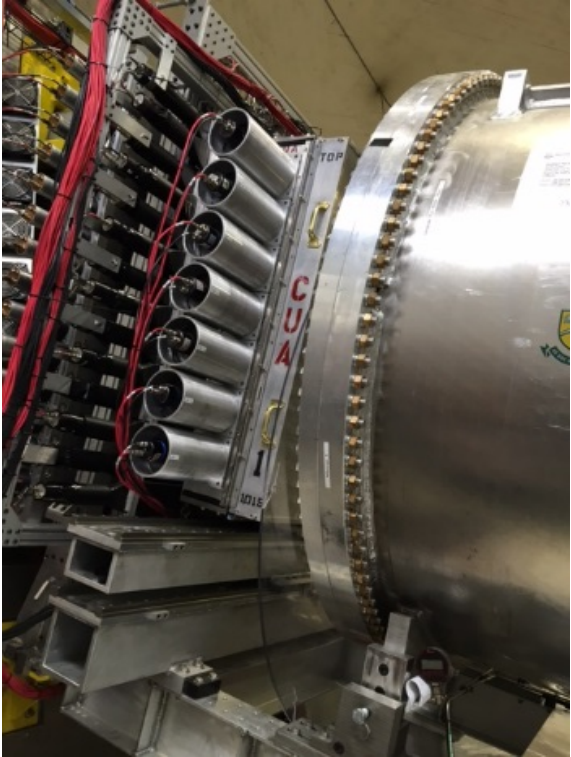


Figure 27: Photograph of the aerogel Čerenkov detector (“CUA” printed on the side of the radiator tray) installed in the SHMS detector stack. To its right is the Heavy Gas Čerenkov. On the left can be seen the edge of the S2XY hodoscope.

The aerogel trays are of the same transverse size as the diffusion box but 11.3 cm (4.45”) deep. The front cover of the trays is made of a 5 mm thick honeycomb panel with effective Aluminum thickness to ~1.3 mm (0.050”). The inner surface of the SP-30 and SP-20 aerogel trays is covered with 0.45 μm thick Millipore paper Membrane GSWP-0010 (Millipore) of reflectivity of about 96% [34]. Though Millipore is difficult to handle, its chemical inertness makes it superior to reflective paints. For the two lower refractive index trays (SP-15 and SP-11), in order to optimize light collection, we used 1 mm thick Gore diffusive reflector material (DRP-1.0-12x30-PSA) with reflectivity of about 99%.

For the Čerenkov radiator high transparency aerogels were used. The higher two of the refractive indices (SP-30 and SP-20) were originally manufactured by Matsushita Electric Works, Ltd. The lower two indices (SP-15 and SP-11) were manufactured by Japanese Fine Ceramics Center. These tiles have dimensions of approximately 11 cm by 11 cm by 1 cm. They feature a wa-

terproof coating that make them hydrophobic [35, 36]. This removes the need for baking (which in fact would destroy the coating). Detailed studies of the aerogel characteristics are presented in Ref. [32].

The trays were filled with aerogel tiles layer by layer. In each layer the tiles were layed down flat and arranged in a brick pattern to minimize holes in the radiator. To fill gaps of less than the size of a full tile at the edges of the tray the aerogel material was cut using a diamond coated saw or razor depending on the refractive index of the material. The aerogel radiator is on average ~9 cm thick (8 layers). The SP-30, SP-20 and SP-15 aerogel trays were filled over their entire 110 cm x 100 cm area. The SP-11 aerogel tray radiator covers only the active area of 90 cm x 60 cm required by the experiments [37, 38, 56, 39, 55]. An inner frame has been designed to arrange the aerogel tiles inside the active area of this tray. The sides of this inner frame are made of carbon fiber square tubes. This assembly allows future X-Y repositioning of the inner frame inside the tray.

To protect the aerogel radiator from severe damage in case of accidental flipping over of a tray during installation, a net of thin stainless steel wires is installed in close proximity to the aerogel surface. This is a technique previously tested in aerogel detectors at JLab [40]. The wires form an interweaving grid by running between stainless steel screws on the sides of the box. Small springs attached to the ends of wires provide necessary tension.

An aerogel tray attaches to the diffusion box by means of bolting through flanges surrounding both boxes. A round O-ring running in a shallow groove along the diffusion box sides ensures a light tight connection. The entire detector is designed so that it can be removed from the sliding detector stand that positions the detector into the SHMS detector stack.

3.8.2. Performance aspects

The light collection performance of the detector was tested with cosmic rays and electron beam. The detector signal shows good uniformity along the vertical (Y) coordinate of the detector surface, but has a significant dependence in the horizontal (X) direction. Possible optimization of this include a variable threshold and an optimized selection of the PMTs installed on the right and left side of the detector. The response of the detector to particles is shown in Fig. 28.

The mean number of photo-electrons in saturation for the tray filled with $n=1.030$ ($n=1.020$) refractive index aerogel is ~10 (~8) which is close to expectation from Monte Carlo simulation. For the trays filled with $n=1.015$ and $n=1.011$ refractive index aerogel, high

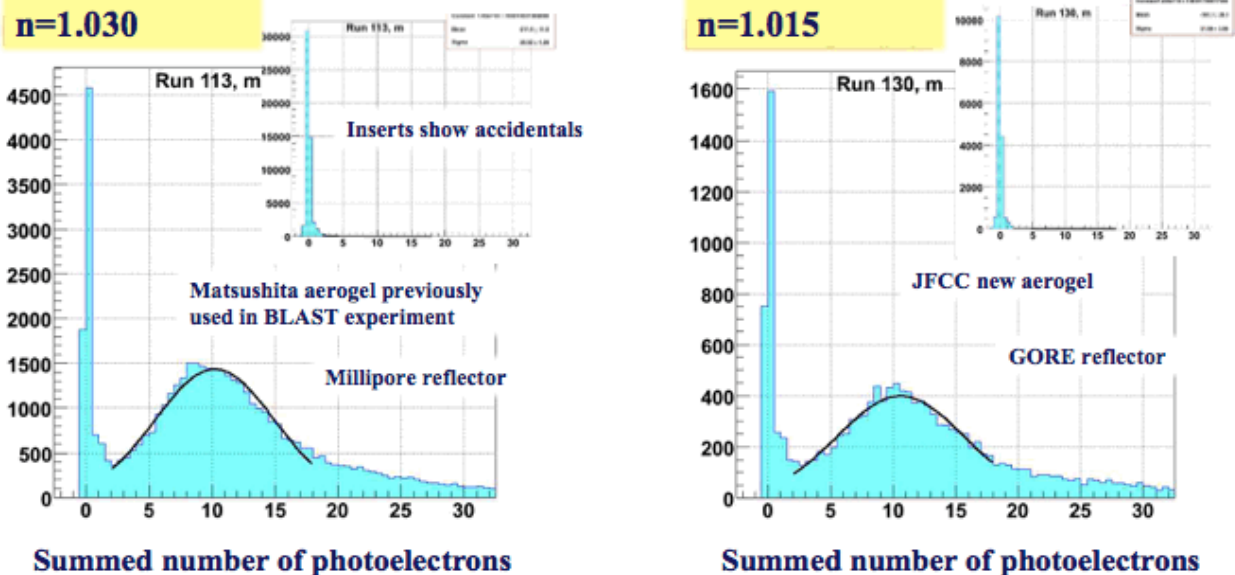


Figure 28: Numbers of photoelectrons observed in the Aerogel Čerenkov.

1097 numbers of photoelectrons were obtained with the use 1123
 1098 of higher reflectivity Gore material to cover the tray, 1124
 1099 ~10 and ~5.5 respectively. This result could be fully 1125
 1100 reproduced by our Monte Carlo simulation by also as- 1126
 1101 suming the aerogel absorption length on the order of 1127
 1102 220 cm. 1128

1103 3.8.3. Results from tests with beam

1104 The performance of the detector was tested with 1130
 1105 beam in Hall C. The detector signal showed good 1131
 1106 uniformity along the vertical direction, but significant 1132
 1107 dependence in the horizontal direction. Possible 1133
 1108 optimizations to address this are discussed below. The 1134
 1109 mean number of photoelectrons in saturation for a tray filled 1135
 1110 with $n=1.030$ refractive index aerogel is 12 photoelec- 1136
 1111 trons and 10 for the tray filled with $n=1.015$ refractive 1137
 1112 index aerogel (see Fig. 28).

1113 3.8.4. Optimizations

1114 Possible optimizations include a variable threshold 1141
 1115 and optimized selection of PMTs. Lower refractive in- 1142
 1116 dex and highly transparent aerogel like that currently 1143
 1117 under investigation by Aspen Aerogel, Inc. may allow 1144
 1118 to provide kaon/proton distinction at even higher parti- 1145
 1119 cle momenta. 1146

1120 3.9. Preshower and Shower Counters

1121 Shower/Preshower Counter section. Author Orga- 1148
 1122 nizer: H. Mkrtchyan, V. Tadevosyan 1149
DRAFT-VI 1150

3.9.1. Preface

In its basic configuration the SHMS detection stack includes a heavy gas Čerenkov for hadron selection, and a noble-gas Čerenkov and lead-glass electromagnetic calorimeter for electron/hadron separation. The detector stack is augmented by aerogel Čerenkov detectors, primarily for kaon identification. The approved experiments demand a suppression of pion background for electron/hadron separation of 1,000:1, with suppression in the electromagnetic calorimeter alone on the level of 100:1. An experiment to measure the pion form factor at the highest Q^2 accessible at JLab with 11 GeV beam requires a strong suppression of electrons against negative pions of a few 1,000:1, with a requirement on the electromagnetic calorimeter of a 200:1 suppression.

Particle detection using electromagnetic calorimeters is based on the production of electromagnetic showers in a material. The total amount of the light radiated in this case is proportional to the energy deposited by the primary particle in the medium. Electrons (as well as positrons and photons), will deposit their entire energy in the calorimeter giving the ratio of energy detected in the calorimeter to particle energy (energy fraction) of one.

Charged hadrons entering a calorimeter have a low probability to interact and produce a shower, and may pass through without interaction. In this case they will deposit a constant amount of energy in the calorimeter. However, they may undergo nuclear interactions in

1152 the radiator (in our case lead-glass) and produce par-
 1153 ticle showers similar to the electron and positron in-
 1154 duced particle showers. Hadrons that interact inelasti-
 1155 cally near the front surface of the calorimeter and trans-
 1156 fer a sufficiently large fraction of their energy to neutral
 1157 pions will mimic electrons. The maximum attainable
 1158 electron/hadron rejection factor is limited mainly by the
 1159 cross section of such interactions.

1160 In this section we describe details of construction
 1161 of the SHMS calorimeter. We present results of pre-
 1162 assembly component checkout, and performance from
 1163 experimental studies.

1164 3.9.2. Construction

1165 As a full absorption detector, the SHMS calorimeter
 1166 is situated at the very end of detector stack of the spec-
 1167 trometer [41]. The relatively large beam envelope of the
 1168 SHMS dictated a design of a wide acceptance cover-
 1169 age. The general requirements for the SHMS calorime-
 1170 ter were:

- 1171 - Effective area: $\sim 120 \times 140 \text{ cm}^2$;
- 1172 - Total thickness: ~ 20 rad. length;
- 1173 - Dynamic range: $1.0 - 11.0 \text{ GeV}/c$;
- 1174 - Energy resolution: $\sim 6\% / \sqrt{E}$, E in GeV ;
- 1175 - Pion rejection: $\sim 100:1$ at $P \gtrsim 1.5-2.0 \text{ GeV}/c$;
- 1176 - Electron detection efficiency: $> 98\%$.

1177 A few different versions of calorimeter assembly for
 1178 the SHMS spectrometer have been considered ([41]) be-
 1179 fore it was optimized for cost/performance.

1180 A possible choice was a construction similar to the
 1181 HMS calorimeter, with radiator from transversely ori-
 1182 ented lead glass blocks and Cerenkov light detection
 1183 from the sides of detector. An alternative was a
 1184 calorimeter similar to HERMES [43] and Hall A [44]
 1185 shower counters.

1186 For each version the energy resolution, electron de-
 1187 tection efficiency and pion/electron separation capabili-
 1188 ties were determined by simulations.

1189 Our studies allowed selection of the optimum
 1190 calorimeter geometry while maintaining the good en-
 1191 ergy resolution and pion rejection capabilities. The
 1192 SHMS calorimeter consists of two parts (see Fig. 29):
 1193 the main part at the rear (Shower), and Preshower before
 1194 the Shower to augment PID capability of the detector.

1195 An optimal and cost-effective choice was found by
 1196 using available modules from HERMES calorimeter for
 1197 Shower part, and modules from the Hall C decommis-
 1198 sioned SOS calorimeter for Preshower. With this choice
 1199 the Shower became 18.2 radiation length deep and al-
 1200 most entirely absorbs showers from $\sim 10 \text{ GeV}$ electro-
 1201 magnetic projectiles, and Preshower became 3.6 radia-
 1202 tion length thick.

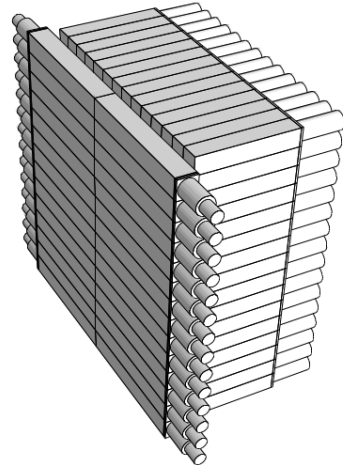


Figure 29: A sketch of SHMS calorimeter. Shown are Preshower (on the left) and Shower parts. Support structures are omitted.

1203 The SHMS Preshower radiator consists of a layer of
 1204 28 TF-1 type lead glass blocks stacked in two columns
 1205 in an aluminum enclosure (not shown in Fig. 29). 28
 1206 PMT assemblies, one per block, are attached to the left
 1207 and right sides of the enclosure. The Shower part con-
 1208 sists of 224 F-101 type lead glass modules stacked in
 1209 a “fly eye” configuration of 14 columns and 16 rows.
 1210 All blocks of Preshower were produced in early 1985-
 1211 1990’s by a Russian factory in Lytkarino [45], whose
 1212 products of good optical quality were well known. \sim
 1213 $120 \times 130 \text{ cm}^2$ of effective area of detector covers the
 1214 beam envelope at the calorimeter.

1215 The Preshower enclosure adds little to the material on
 1216 the pass of particles. On the front and back are 2" Hon-
 1217 eycomb plate and a 1 mm sheet of aluminum respec-
 1218 tively, which add up to 1.7% of radiation length only.
 1219 The optical insulation of the $10 \text{ cm} \times 10 \text{ cm} \times 70 \text{ cm}$ TF-
 1220 1 blocks in the Preshower is optimized to minimize the
 1221 dead material between them, without compromising the
 1222 light tightness. First, the blocks are loosely wrapped in a
 1223 single layer of $50 \mu\text{m}$ thick reflective aluminized Mylar
 1224 film, with Mylar layer facing the block surface. Then,
 1225 every other block is wrapped with a 10 cm wide strip
 1226 of $50 \mu\text{m}$ thick black Tedlar film, to cover its top, bot-
 1227 tom, left and right sides but the circular openings for the
 1228 PMT attachments. Looking at the face of detector, the
 1229 wrapped and unwrapped blocks are arranged in a chess
 1230 pattern. Insulation of the remaining front and back sides
 1231 of the blocks are provided by facing inner surfaces of the
 1232 front and rear plates of the enclosure, covered also with
 1233 Tedlar. In addition, a layer of Tedlar separates the left

1234 and the right columns.

1235 The PMT assembly tubings are screwed in \varnothing 90 mm 1287
1236 circular openings on both sides of the enclosure. The 1288
1237 spacing of the openings matches the height of the 1289
1238 blocks, so that a PMT faces to each of the blocks. The 1290
1239 3" XP3462B PMTs are optically coupled to the blocks 1291
1240 using ND-703 type Bycron grease of refractive index 1291
1241 1.46. 1292

1242 The HERMES modules used in the Shower part are 1293
1243 similar in construction to the HMS but differ in details. 1294
1244 The radiator is an optically isolated $8.9 \times 8.9 \times 50$ cm³ 1295
1245 block of F-101 lead-glass, which is similar to TF-1 in 1296
1246 physical parameters. The typical density of F-101 type 1297
1247 lead-glass is 3.86 g/cm³, radiation length 2.78 cm, and 1298
1248 refraction index 1.65. 1299

1249 Results of TF-1 and F-101 type lead-glass blocks 1300
1250 transmittance measurements are presented in [41]. 1301

1251 Each F-101 block is coupled to a 3" XP3461 PMT 1302
1252 from Photonis, with green extended bialkali photocath- 1303
1253 ode, of the same sizes and internal structure as the 1304
1254 XP3462B in the Preshower. Typical quantum efficiency 1305
1255 of the photocathode is $\sim 30\%$ for $\lambda \sim 400$ nm light, and 1306
1256 the gain is $\sim 10^6$ at ~ 1500 V. Silgard-184 silicone glue 1307
1257 of refractive index 1.41 is used for optical coupling of 1308
1258 the PMTs to lead-glass blocks. 1309

1259 A μ -metal sheet of 1.5 mm thickness and two layers 1309
1260 of Teflon foil are used for magnetic shielding and elec- 1310
1261 trical insulation of the PMTs. The blocks are wrapped 1311
1262 with 50 μ m aluminized Mylar and 125 μ m black Tedlar 1312
1263 paper for optical insulation. A surrounding aluminum 1313
1264 tube which houses the μ -metal, is fixed to a flange, 1314
1265 which is glued to the surface of the lead-glass. The 1315
1266 flange is made of titanium, which matches the thermal 1316
1267 expansion coefficient of F-101 lead-glass [42]. 1317

1268 Beyond simple repairs, no adjustment has been made 1318
1269 to the original HERMES construction of the modules 1319
1270 for re-use in the SHMS calorimeter. 1320

1271 As both the TF-1 and F-101 lead-glass blocks have 1321
1272 been in use for more than 14 years under conditions of 1322
1273 high luminosity, there was concern about possible radi- 1323
1274 ation degradation of the blocks and the PMTs. 1324

1275 The changes in transparency of TF-1 and F-101 type 1325
1276 lead-glass radiators have been studied. The estimated 1326
1277 radiation dose for the used blocks was about 2 krad. For 1327
1278 several samples of F-101 and TF-1 type blocks the light 1328
1279 transmittance has been measured before and after 5 days 1329
1280 of curing with UV light (of wavelength $\lambda=200$ -400 nm). 1329

1281 We did not find notable degradation in transmittance 1330
1282 for the TF-1 type blocks taken from the SOS calorimeter 1331
1283 and F-101 blocks taken from HERMES detector. 1332

1284 The gain and relative quantum efficiencies for 1333
1285 randomly selected PMTs from the SOS calorimeter 1334

(XP3462B) and from the HERMES detector (XP3461) 1286
1287 have been measured to check possible degradation ef- 1288
1289 fects in the PMTs. A ~ 10 -15% systematic decrease in 1290
1291 quantum efficiency was noticed.

3.9.3. Photomultiplier tube selection and studies

The SHMS Preshower inherited PMTs from the re-tired SOS calorimeter. The choice of XP3462B PMT for Hall C calorimeters was made in 1994 after studies of several other 3 inch and 3.5 inch photomultiplier tubes on the matter of having good linearity, photocathode uniformity, high quantum efficiency, and good timing properties. Gain variations with HV and dark currents also were measured [46]. For samples of PMTs the photocathode uniformity and effective diameter have been studied with a laser scanner. Following these tests, as a time and cost effective solution, a 3" diameter (≈ 68 mm) semitransparent bi-alkaline photocathode, Photonis XP3462B PMTs were chosen for the equipment of the JLab Hall C calorimeters. These 8-stage PMTs have a linear focused cube dynode structure with a peak quantum efficiency (QE) of $\sim 29\%$ at 400 nm.

3.9.4. Studies on optical properties of TF-1 type lead glass blocks

With its index of refraction ~ 1.65 , radiation length 2.74 cm and density of 3.86 g/cm³ TF-1 type lead glass is well suited for serving as Čerenkov radiator in electromagnetic calorimeters. The fractional composition consists primarily of PbO (51.2%), SiO₂ (41.3%), K₂O (3.5%) and Na₂O (3.5%).

The light transmittance of TF-1 type lead-glass blocks for the SHMS Preshower was checked in 2008 using a spectrophotometer from the JLab Detector Group [47]. The wave-length was scanned from 200 nm to 700 nm in steps of 10 nm. The blocks were oriented transversely, and the light intensity passing through the 10 cm thickness was measured. The results were compared with measurements from 1992, before assembling of calorimeters for the Hall C HMS/SOS spectrometers. Reliability of the measurements was checked by measuring spared, unused blocks and comparing again with 1992 data. From comparison of 1992 and 2008 data, signs of marginal degradation has been noticed.

3.9.5. Choice and studies of PMT bases

The Preshower PMT high voltage base design is optimized for the requirements of good linearity (better than 1%), high rate capability and a weak variation of PMT gain with anode current [46].

A design, which is a purely resistive, high current (2.3 mA at 1.5 kV), surface mounted divider

($\sim 0.640 M\Omega$), operating at negative HV is selected. The relative fractions of the applied HV between the dynodes (from cathode to anode) are: 3.12/1.50/1.25/1.25/1.50/1.75/2.00/2.75/2.75. The supply voltage for a gain of 10^6 is approximately 1750 V.

The PMT resistive base assembly is linear to within $\sim 2\%$ up to the peak anode current of $120 \mu\text{A}$ ($\sim 5 \times 10^4$ pe). The dark current is typically less than 3 nA. The base has anode and dynode output signals.

3.9.6. Monte Carlo simulations

Prior to construction, the designed calorimeter setup was computer simulated in order to possibly optimize the setup and get predictions for key characteristics.

The simulations were based on the GEANT4 package [48], release 9.2. As in the simulations of the HMS calorimeter (see [41]), the QGSP_BERT physics list was chosen to model hadron interactions [49]. The code closely followed the parameters of the detector components. Other features are added into the model in order to bring it closer to reality, such as: light attenuation length in the lead glasses and its block to block variation according to our measurements; PMT quantum efficiencies from the graphs provided by vendor, passive material between the spectrometer focal plane and the calorimeter; sampling of incoming particles at the focal plane of the spectrometer. The Čerenkov light propagation and detection was handled by a custom code, in approximation of strict rectangular geometry of the lead glass blocks with perfectly polished surfaces. Light reflection and absorption by the Mylar wrapping was modeled via Aluminum complex refractive index, with Mylar support facing the block, and a thin air gap between the wrapping and the block. Both light passage to the PMT photocathode through the optical grease and the PMT window, and reflections from the block sides were modeled in approximation of thin dielectric layers ([50], p. 360). The electronic effects, such as pedestal widths and channel to channel PMT gain variations were assumed as for the HMS calorimeter before the 12 GeV modifications.

The simulations reveal no flaws in the design construction of the SHMS calorimeter, and performance similar to other lead glass based calorimeters. The studies indicated gain in pion suppression on the order of several times from combining signal from Preshower with total energy deposition in the calorimeter.

3.9.7. Cabling and electronics

The analog signals from the PMTs of the calorimeter are digitized in the 16 channel JLab FADC250 modules,

located in the electronics hut adjacent to the SHMS detector hut. The analog signals are transported to FADCs via $\sim 30'$ long RG58 type cables laid down in a conduit in the wall of the SHMS shield house. The digitized signals are sent further to the Hall C counting house for the input to the DAQ system via ??' long ?? type multi-fiber cables. The early digitization allows avoid noise overlap during long distance signal transportation from the experimental hall to the counting house.

During routine experimental data taking the FADCs are operated in the Integral mode, when the pedestal level is computed and subtracted from the pulse signal on event by event basis, and integrated in a programmable time window signal is provided. However, for the debugging purposes or for DAQ tuning the FADCs can be operated in the Pulse mode. In this case entire pulse samples are available for analysis.

Before being fed to FADCs, the analog signals from the Preshower are split in 50:50 ratio for the purpose to organize fractional sums of signals from the Preshower modules for the trigger. The relatively short 30' cables from the Preshower PMTs to the FADCs (compare to 47' long cables from the hodoscope PMTs to the Hut Patch Panel) allowed to compensate delay time when forming the sums in the Linear FAN-IN/OUT Summing Module. The SUM signals are set up as follows:

1. Preshower Sum(1-4) = NEG(1-4) + POS(1-4)
2. Preshower Sum(5-8) = NEG(5-8) + POS(5-8)
3. Preshower Sum(9-12) = NEG(9-12) + POS(9-12)
4. Preshower Sum(13-14) = NEG(13-14) + POS(13-14)

Here NEG and POS denote signals from right and left sides of the Preshower. Combination of modules for each sum can be changed if needed. These partial sum signals are discriminated in a NIM discriminator and sent to the Counting room via patch panel in the SHMS hut and $\sim 404'$ long (489.28 ns) RG8 type cables. In the electronic room they are used to form Preshower Low (PSh Lo) and Preshower High (PSh Hi) trigger signals.

3.9.8. Calorimeter Calibration

The ability of particle identification of a calorimeter is based on differences in the energy deposition from different types of projectiles. The deposited energy is obtained by converting the recorded ADC channel value of each module into equivalent energy.

The data analysis procedure corrects for the gain differences in the process of calorimeter calibration. Good electron events are selected by means of gas Čerenkov detector. The standard calibration algorithm [51] is

1433 based on minimization of the variance of the estimated
 1434 energy with respect to the calibration constants, subject
 1435 to the constraint that the estimate is unbiased (relative
 1436 to the primary energy). The momentum of the primary
 1437 electron is obtained from the tracking in the magnetic
 1438 field of the spectrometer.

The deposited energy per channel is estimated by

$$e_i = c_i \times A_i, \quad (6)$$

1439 where i is the channel number, c_i is the calibration constant,
 1440 A_i is the FADC pulse integral signal. Note that the
 1441 Preshower signals are corrected for the light attenuation
 1442 dependence versus horizontal hit coordinate y .

1443 In the calorimeter analysis code hits on adjacent
 1444 blocks in the Preshower and in the Shower are grouped
 1445 into clusters. For each cluster the deposited energy
 1446 and center of gravity are calculated. These clusters
 1447 are matched with tracks from the upstream detectors
 1448 if the distance from the track to cluster is less than a
 1449 predefined “slop” parameter (usually 7.5 cm). For the
 1450 Preshower the distance is calculated in the vertical di-
 1451 rection. 1480

1452 The calorimeter energy corresponding to a track is 1482
 1453 divided by the track momentum and used for particle 1483
 1454 identification. In the few GeV/c range pions and elec- 1484
 1455 trons are well separated (see Fig. xxxx, NEED FIG- 1485
 1456 URE), a cut at 0.7 ensures an electron detection effi- 1486
 1457 ciency ~99% and pion suppression of tens of times. 1487

1458 3.9.9. Performance of SHMS calorimeter 1488

1459 The performance of the SHMS calorimeter under 1489
 1460 the beam conditions was tested first time during 12 1490
 1461 GeV Hall C Key Performance Parameter Run in spring 1491
 1462 of 2017. As part of the SHMS detector package the 1492
 1463 calorimeter was commissioned in the Hall C fall run 1493
 1464 period of the same year. The first experimental data 1494
 1465 with use of the calorimeter is being collected for 1495
 1466 series of the first 12 GeV Hall C experiments: E12- 1496
 1467 10-002 (F_2 structure function at large x) [52], E12- 1497
 1468 06-107 (Search for Color Transparency) [55], E12-10- 1498
 1469 008 (EMC effect) [53], E12-10-003 (Deuteron Electro- 1499
 1470 Disintegration) [54], E12-09-017 (P_t dependence of 1500
 1471 SIDIS cross section) [56], E12-09-002 (Precise π^+/π^- 1501
 1472 ratios in SIDIS) [57] and E12-09-011 (L/T separated 1502
 1473 $p(e, e'K)$ factorization test) [38]. The early analyses 1503
 1474 of the calorimetric data demonstrate satisfactory perfor- 1504
 1475 mance of the detector in terms of resolution and PID 1505
 1476 capabilities (fig. 30).

1477 3.9.10. Summary on the SHMS calorimeter

1478 Design, construction details and performance of the 1505
 1479 electromagnetic calorimeter for the newly built SHMS 1506

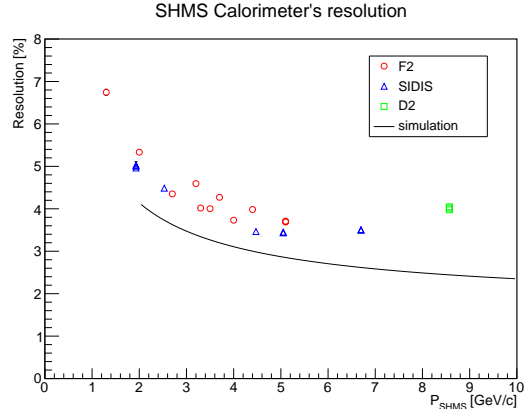


Figure 30: Resolution of the SHMS calorimeter from calibrations of runs from the Spring 18 run period. The solid line is result from the early simulations. [This figure is not final.]

spectrometer in Hall C has been presented. From a few considered versions, the Preshower+Shower configuration was selected as most cost-effective. The Preshower consists of a layer of 28 modules with TF-1 type lead glass radiators, stacked back to back in two columns. The Shower part consists of 224 modules with F-101 type lead glass radiators, stacked in a “fly eye” configuration of 14 columns and 16 rows. $120 \times 130 \text{ cm}^2$ of active area covers beam envelope at the calorimeter.

The calorimeter was commissioned as part of the SHMS detector package in the fall of 2017, then used in the first 12 GeV Hall C experiments in 2018. The first calorimetric data show satisfactory performance of the detector.

3.10. Trigger and Data Acquisition

Trigger and DAQ section. Author Organizer: B. Sawatzky

3.10.1. DAQ Hardware/Software

- Brief description of CODA w/ references
 - Block diagram of ROC layout; comment on potential 3rd arms, etc
- Brief description of primary payload modules in use (w/ refs). Pipeline capable, multihit, integrated scalers, in-house FPGA-based programming capabilities, etc.
 - JLab F250 module (comment/ref supporting modules: TI/TM, SD, STP, ...)

- 1507 – CAEN 1190 module (comment on support- 1543
 1508 ing hardware) 1544
 1509 – JLab style VXS crate 1545
- 1510 • Table w/ detectors, channel counts, and what 1546
 1511 is measured (ADC, TDC(fADC), TDC(1190), 1547
 1512 scaler(fADC/hardware). 1548
 1513 • Comment on radiation shielding/considerations for 1549
 1514 Hall C electronics 1550
- 1515 – Reference detector hut construction/shielding 1551
 1516 – Reference/outline RG-8 signal and HV lines 1552
 1517 to CH upper floors 1553
- 1518 • Grounding/Shielding considerations 1554
- 1519 **3.10.2. Online Hall C Computing Environment**
 1520 • Brief outline of capabilities/hardware/network 1555
 1521 • Outline recommended online data workflow 1556
 1522 • ... 1557
- 1523 **3.10.3. Standard Triggers**
 1524 Layout basic “legacy” trigger philosophy, simple 1563
 1525 block diagrams. 1564
- 1526 • Pre-triggers 1565
 1527 • PID leg composition/construction 1566
 1528 • ... 1567
- 1529 **3.10.4. Electronic Deadtime Measurement System (EDTM)**
 1530 Outline EDTM system, capabilities, and vetting (w/ 1571
 1531 support from Pooser, Mack, et al). Summarize and ref- 1572
 1532 erence future NIM article perhaps? 1573
- 1533 **3.10.5. Auxiliary Data Collection**
 1534 • EPICS logging 1574
 1535 • Spectrometer angle measurement 1575
 1536 • Payload module configuration data 1576
 1537 • BPM, BCM, Charge asymmetry, etc. 1577
 1538 • Scalers 1578
 1539 • Alarm handler(?) 1579
- 1540 • ... 1580
- 1541 **3.10.6. Future Plans / Pipeline trigger**
 1542 • Complete migration of legacy VxWorks con- 1581
 1543 trollers to Intel boards 1582
 1544 • Reference near-term expansion plans (for 1583
 1545 NPS/LAD/CGEN). Significant increase in 1584
 1546 FADC/TDC/HV channel counts are relevant to 1585
 1547 future systems. 1586
 1548 • Outline future plan to implement and verify fully 1587
 1549 pipelined trigger w/ projected capabilities. 1588
 1550 • ...
- 1551 **3.11. Software**
 1552 Hall C Data is analyzed by the Hall C analysis pack-
 1553 age hcana. This package does full event reconstruc-
 1554 tion for the SHMS when used alone or in coincidenc-
 1555 e with other detectors. hcana is based on the modular
 1556 Hall A analyzer [58] ROOT [59] based C++ analysis
 1557 framework. This framework provides for run-time user
 1558 configuration of histograms, ROOT tree contents, cuts,
 1559 parameters and detector layout.
 1560 hcana includes C++ classes for detectors, spec-
 1561 trometers, and physics analyses. Instantiation of these
 1562 classes as objects is configured at run-time through a
 1563 ROOT script which also sets up the configuration of
 1564 analysis replay. Due to the similarity of the SHMS
 1565 and HMS spectrometers and their detector packages, the
 1566 same spectrometer and detector classes are used for both
 1567 spectrometers. For example, the drift chamber package
 1568 class is instantiated for both spectrometers with each ob-
 1569 ject configured by its specific parameters and geometry.
 1570 Additional modules such as new front end decoders, de-
 1571 tectors, or physics analysis modules can easily be added
 1572 to hcana. These modules can either be compiled into
 1573 the analyzer or be compiled separately and dynamically
 1574 loaded at run-time.
 1575 Event analysis is segmented into 3 steps of spectrom-
 1576 eter and detector specific analysis.
 1577 1. Decoding: Detector requests from the low level
 1578 decoder a list of hits sorted by plane and counter
 1579 number. A minimal amount of processing is done
 1580 to make data available for low level histograms.
 1581 2. Coarse Processing: Tracks are found in the drift
 1582 chambers. Hits and clusters in the hodoscope,
 1583 shower counter, and other detectors are matched
 1584 to the tracks to determine time-of flight. Various
 1585 detectors provide information for particle identifi-
 1586 cation.

1589 3. Fine processing: Particle identification informa- 1636
1590 tion is refined, tracks in the focal plane are traced 1637
1591 back to the target coordinate system and particle 1638
1592 momentum is determined. 1639

1593 Each step of these steps is completed for all detectors 1640
1594 before proceeding to the next step. Some limited infor- 1641
1595 mation is passed between detectors at each step. For ex- 1642
1596 ample, timing information from the hodoscopes is used 1643
1597 to obtain the start time for the the drift chambers in the 1644
1598 decoding step and tracks obtained from the drift cham- 1645
1599 bers are associated with shower counter hit clusters in 1646
1600 the fine processing step. 1647

1601 After these steps, single arm and coincidence physics 1647
1602 quantities are calculated using various physics analysis 1648
1603 classes that are configured at run-time. 1649

1604 3.12. *Online Monitoring*

1605 After each data taking run (typically an hour or less) 1650
1606 is started, a subset of the data is analyzed with hcana. 1651
1607 An easily configurable histogram display GUI is used to 1652
1608 view diagnostic histograms and compare them to refer- 1653
1609 ence histograms.

1610 Occupancies and multiplicites for each detector de- 1654
1611 tector system are monitored in order to determine the 1655
1612 health of each channel in the detector stack. A variety 1656
1613 of variables associated with particle identification, focal 1657
1614 plane distributions, and reconstructed target variables are 1658
1615 also monitored to ensure the SHMS is functioning nom- 1659
1616 inally. 1660

1617 The EPICS [60] control system alarm handler is used 1661
1618 to monitor experiment settings and beam conditions. 1662
1619 This includes spectrometer magnet settings, detector 1663
1620 high voltages, drift chamber gas, cryogenic systems and 1664
1621 spectrometer vacuum. 1665

1622 4. SHMS Performance: Operating Experience and 1664 1623 Commissioning Results

1624 *System Performance section. Organizer: H. Fenker –* 1665
1625 *with input from all authors.* 1666

1626 Each subsection author (above) is asked to provide 1667
1627 suggestions, figures, and text snippets or complete sub- 1668
1628 sections that can be put together to create this section 1669
1629 of the paper. The purpose of this section is to present 1670
1630 the demonstrated capabilities of the SHMS – at least in 1671
1631 comparison to its design specifications. 1672

1632 4.1. *Acceptance*

- 1633 1. vs. delta
- 1634 2. vs. theta, phi
- 1635 3. vs. $x_{\text{targ}}, y_{\text{targ}}, z_{\text{targ}}$

4.2. *Rates and Livetime*

1. Deadtime Measurement by Electronic Pulse Generator
2. Trigger rate vs. beam current
3. Event rate vs. beam current
4. Data rate vs. beam current
5. Consistency of livetime determination

4.3. *Measurement Precision*

1. Momentum
2. Angle
3. Recoil mass spectrum
4. Missing mass from $H(e^- e^+)p$
5. Magnitude and Impact of Multiple Scattering. Removal of NGC to improve low-energy precision.

4.4. *Stability and Reproducibility*

1. Trigger rate
2. Kinematic quantities
3. Trigger efficiency

4.5. *System Efficiency*

(as opposed to individual detector efficiency which should go in the detector subsection above.)

1. Track finding and fitting
2. Particle ID / Rejection
3. Background Rejection / Accidental rate / Amount and Impact of delta-ray production

5. Conclusion

Conclusion section. Author Organizer: H. Fenker

- We wanted to build it
- We built it
- It works
- We're using it to do physics

- [1] Hall-C Collaboration, JLab Internal Document - (2002).
- [2] Physics & Instrumentation with 6-12 GeV Beams, a Thomas Jefferson National Accelerator Facility report, S. Dytman, H. Fenker and P. Roos, eds., June 1998.
- [3] References to SHMS magnet conference papers and/or publications or tech-notes.
- [4] I. Niculescu et al., Phys. Rev. Lett. 85 (2000) 1186;
- [5] T. Kitagaki, et al., Phys. Rev. D 42 (1990) 1331; A. Bergier, et al., Z. Phys. C 5 (1980) (265), and references therein.
- [6] J. R. Dunning et al., Phys. Rev. 141 (1966) 1286; R. Bilger, et al., Nucl. Inst. and Meth. A 457 (2001) 64; I. Lehmann, et al., Nucl. Instr. and Meth. A 530 (2004) 275; A. Klimenko, et al., Phys. Rev. C 73 (2006) 035212.

- [7] The ALICE Transition Radiation Detector: Construction, operation, and performance, ALICE Collaboration, Nucl. Inst. and Meth. A 888 (2018) 88-127; doi:10.1016/j.nima.2018.02.027.
- [8] The G0 Experiment, D. Androic, et al., Nucl. Inst. and Meth. A 646 (2011) 59-86; doi:10.1016/j.nima.2011.03.020.
- [9] The HERMES Spectrometer, K. Ackerstaff, et al., Nucl. Inst. and Meth. A 417 (1998) 230-265; doi:10.1016/S0168-9334(98)00012-2.
- [10] A forward magnetic spectrometer system for high-energy heavy-ion experiments, K. Shigaki, et al., Nucl. Inst. and Meth. A 438 (1999) 282-301; doi:10.1016/S0168-9334(99)00012-2.
- [11] CLAS, B. Mecking, et al., Nucl. Inst. and Meth. A 503 (2003) 513-553; doi:10.1016/j.nima.2003.03.011.
- [12] The aerogel threshold Cherenkov detector for the High Momentum Spectrometer in Hall C at Jefferson Lab, R. Asaturyan, et al., Nucl. Inst. and Meth. A 548 (2005) 364-374; doi:10.1016/j.nima.2005.01.011.
- [13] The Aerogel Čerenkov counter for the SHMS magnetic spectrometer in Hall C at Jefferson Lab, T. Horn, et al., Nucl. Inst. and Meth. A 842 (2017) 28-47; doi:10.1016/j.nima.2017.01.001.
- [14] T. Skwarnicki, NIM A553 (2005) 339-344; M. Artuso et al., NIM A558 (2006) 373-387. doi:10.1016/j.nima.2005.09.011.
- [15] ASM Aerospace Specification Metals, 14112 Pontiavoy Ave., Santa Fe Springs, CA. doi:10.1016/j.nima.2006.01.001.
- [16] Sinclair Glass, 105 N. Wabash Ave., Hartford City, IN. doi:10.1016/j.nima.2006.01.001.
- [17] W. Li, M.Sc. thesis, University of Regina, 2012. doi:10.1016/j.nima.2006.01.001.
- [18] Corning International, 1 Riverfront Plaza, Corning, NY. doi:10.1016/j.nima.2006.01.001.
- [19] Hamamatsu Photonics K.K., Electron Tube Division, 314-5 Shimokanzo, Iwata City, Ahizuoka Pref., Japan. doi:10.1016/j.nima.2006.01.001.
- [20] Evaporated Coatings Inc., 2365 Maryland Rd., Willow Grove, PA. doi:10.1016/j.nima.2006.01.001.
- [21] E.J Brash et al, NIM A487 (2002) 346-352. doi:10.1016/j.nima.2002.06.001.
- [22] Ruggero Turra, CERN, (2009). doi:10.1016/j.nima.2009.01.001.
- [23] T. Horn, *SHMS Shielding Design*, JLab Hall C Document Database 392-v1 (19 Nov 2008); *Final SHMS Shielding Design*, JLab Hall C Document Database 595-v1 (24 Sept 2009).
- [24] P. J. Griffin et al., *The role of thermal and fission neutrons in reactor neutron-induced upsets in commercial SRAMs*, IEEE NS Vol. 44, No. 6, Dec. 1997. doi:10.1016/j.nima.2006.01.001.
- [25] C. I. Underwood, *The Single-Event-Effect Behaviour of Commercial-Off-The-Shelf Memory Devices - A Decade in the Low-Earth orbit*, IEEE Transactions on Nuclear Science Vol. 45, No. 3, June 1998. doi:10.1016/j.nima.2006.01.001.
- [26] W. R. Leo, *Techniques for Nuclear and Particle Physics Experiments*, second edition, Springer Verlag Berlin, Heidelberg 1987, 1994. doi:10.1016/j.nima.2006.01.001.
- [27] J. F. Briesmeister (ed.), MCNP - A General Monte Carlo N-particle Transport Code Version A, LA-12625-M, Los Alamos National Laboratory, Los Alamos, New Mexico (1993). doi:10.1016/j.nima.2006.01.001.
- [28] S. Wood, private communication (2008). doi:10.1016/j.nima.2006.01.001.
- [29] M. Jones et al., private communication (2008). doi:10.1016/j.nima.2006.01.001.
- [30] Birenbaum et al., Phys. Rev. C51, (1995) 3496. doi:10.1016/j.nima.2006.01.001.
- [31] D. Marsh , *Particle Practice Concrete Products* Vol. 117, no. 2 (2014) 40. doi:10.1016/j.nima.2006.01.001.
- [32] T. Horn, et al., The Aerogel Čerenkov detector for the SHMS magnetic spectrometer in Hall C at Jefferson Lab, Nucl. Instrum. Meth. A842 (2017) 28-47. arXiv:1607.05264, doi:10.1016/j.nima.2016.10.039. doi:10.1016/j.nima.2017.01.001.
- [33] Gore, W. L. & Associates INC., "", http://www.gore.com. doi:10.1016/j.nima.2006.01.001.
- [34] Millipore Corporation, 80 Ashly Road, Bedford, MA 01730, "", http://www.millipore.com/. doi:10.1016/j.nima.2006.01.001.
- [35] I. Adachi, et al., Study of highly transparent silica aerogel as a RICH radiator, Nucl. Instrum. Meth. A553 (2005) 146-151. doi:10.1016/j.nima.2005.08.022. doi:10.1016/j.nima.2005.08.022.
- [36] E. Aschenauer, et al., Optical characterization of n = 1.03 silica aerogel used as radiator in the RICH of HERMES, Nucl. Instrum. Meth. A440 (2000) 338-347. doi:10.1016/S0168-9334(00)00023-7.
- [37] Horn T., Huber G.M., and others, "scaling study of the l-t separated pion electroproduction cross section at 11 gev", approved Jefferson Lab 12 GeV Experiment (2007).
- [38] T. Horn, G. M. Huber, P. Markowitz, et al., Spokespersons, Studies of the L-T Separated Kaon Electroproduction Cross Section from 5-11 GeV. JLab proposal E12-09-011..
- [39] Bosted P., Ent R., Kinney E., Mkrtchyan, H., and others, "Measurement of the Ratio $r = \sigma_l/\sigma_t$ in Semi-Inclusive Deep-Inelastic Regimes", approved Jefferson Lab 12 GeV Experiment (2006).
- [40] R. Asaturyan, et al., The aerogel threshold Čerenkov detector for the high momentum spectrometer in Hall C at Jefferson Lab, Nucl. Instrum. Meth. A548 (2005) 364-374. arXiv:physics/0411147, doi:10.1016/j.nima.2005.04.058.
- [41] H. Mkrtchyan et al., Nucl. Instrum. Meth. A **719** (2013) 85-100.
- [42] H. Avakian et al., Nucl. Instrum. Meth. A **378** (1996) 155-161.
- [43] H. Avakian et al., Nucl. Instrum. Meth. A **417** (1998) 69-78.
- [44] J. Alcorn et al., Nucl. Instrum. Meth. A **522** (2004) 294.
- [45] Lytkarino factory of optical glasses, 140061, Lytkarino, Moskow region, Russia.
- [46] T. Amatuni, G. Kazaryan, H. Mkrtchyan, V. Tadevosyan and W. Vulcan, Nucl. Instr. Meth. A **374**, 39-47 (1996).
- [47] C. Zorn, private communication.
- [48] S. Agostinelli et al., GEANT4—a simulation toolkit. Nucl. Instrum. Meth. A **506** (2003) 250-303; J. Allison et al., IEEE Transactions on Nuclear Science **53**, No.1, (2006) 270-278.
- [49] John Apostolakis et al., Progress in hadronic physics modeling in GEANT4. XIII Int. Conf. on Calorimetry in High Energy Physics. (CALO2008); J. of Phys. Conf. Series **160** (2009) 012073; J. Apostolakis et al., Hadronic Shower Shape Studies in GEANT4, CERN-LCGAPP-2007-02.
- [50] M. Born, E. Wolf. Principles of Optics. Pergamon Press, 1965.
- [51] Ts. Amatuni, On the calibration of segmented full absorption calorimeters. Unpublished.
- [52] Precision measurements of the F_2 structure function at large x in the resonance region and beyond, JLab Proposal E12-10-002, S. Malace, M. Christy, C. Keppel, M. Niculecu spokespersons.
- [53] Detailed studies of the nuclear dependence of F_2 in light nuclei, JLab Proposal E12-10-008, D. Gaskell, J. Arrington, A. Daniel, N. Fomin spokespersons.
- [54] Deuteron Electro-Disintegration at Very High Missing Momentum, JLab Proposal E12-10-108, W. Boeglin, M. Jones spokespersons.
- [55] D. Dutta, R. Ent., et al. Spokespersons, "The Search for Color Transparency at 12 GeV", approved Jefferson Lab 12 GeV Experiment (2006).
- [56] R. Ent, P. Bosted, E. Kenney, H. Mkrtchyan spokespersons, "Transverse Momentum Dependence of Semi-Inclusive Pion Production", approved Jefferson Lab 12 GeV Experiment (2009).
- [57] Precise Measurement of π^+/π^- Ratios in Semi-inclusive Deep Inelastic Scattering Part I: Charge Symmetry violating Quark Distributions, JLab Proposal E12-09-002, K. Hafidi, D. Dutta, D. Gaskell spokespersons.
- [58] Hall A Analyzer, <https://hallaweb.jlab.org/podd/>.
- [59] Rene Brun and Fons Rademakers, ROOT - An Object Oriented Data Analysis Framework, Proceedings AIHENP'96 Workshop, Lausanne, Sep. 1996, Nucl. Instrum. Meth. A **389** (1997) 81-86. See also <http://root.cern.ch/>.
- [60] EPICS reference here.

1807 *Notes for All Authors.*

1808

1809

1810

1811

1812

Nuclear Instruments and Methods Format: NIM-

A is a two-column journal, but they require that papers be submitted in their single-column preprint style, with line numbers.

1813

1814

1815

1816

1817

1818

1819

1820

1821

1822

1823

1824

1825

1826

1827

1828

1829

1830

1831

1832

1833

1834

1835

1836

1837

1838

1839

1840

1841

1842

1843

1844

1845

1846

1847

1848

1849

1850

1851

1852

1853

1854

1855

1856

1857

1858

At submission time, Elsevier will want the image files and references to be named sequentially. Elsevier wants

a lot of stuff done their way. I'll take care of that. I just ask that you send me the bare .tex of your subsection, along with pdf image files, so that it will compile when it gets pulled-in by the \input statement in my top-level shmsNIM.tex file.

AGAIN: Please do not waste time by creating your own stand-alone .tex document. The L^AT_EX styles,

macros, etc. that are used **must be those provided by the publisher.** To check your .tex, put it in the skeleton file that I provided to you – the one that resides inside the directory that I created for your **subsection**. Then, from within the nimtex directory, run 'make' on the file shmsNIM.tex. This will compile all of the .tex files for the whole article, including your own file, and it will allow you to verify that the .tex you have written is compatible with the overall document and with the publisher's stylesheet.

Normally you would only modify files that are within your subdirectory. The one exception is the file bib_items.tex – you can add entries to that file if you surround what you add with a pair of comment lines giving your name and the date you added the content. Send author/affiliation information to me and I will add it to the front matter.

I (hcf) have included references to several archival NIM articles [7, 8, 9, 10] to see how other authors have documented their detector systems. Some of them describe hardware at Jefferson Lab [11, 12].

One can see in Fig. 31, below, how to include a pdf image file for use as a single-column-width figure within this document. Fig. 43 shows the same image included as a full-page-width figure. Also included is an example of making a table. See Table 6.

File Organization: Under the top-level directory nimtex I have created a subdirectory for each section or subsection of the paper. In each of those you'll find a .tex file ready for authors to begin writing. To keep us from clobbering each other by accidentally duplicating a file name, I suggest that you put your .pdf graphic files (yes: please supply pdf files for all graphics) and any other content files inside the subdirectory containing your .tex file. Since the make will be run from the top-level directory, remember to reference the subdirectory path to the graphic (or other) file when you

1859 \include it from the .tex file. Please examine THIS file
1860 ("Instructions_For_Authors.tex") to see how the
1861 figures herein are referenced.

1862 **Sending New Material:** When you want to submit
1863 new or revised material for inclusion in the overall NIM
1864 article, all you have to do is email the .tex and .pdf files
1865 in your subsection directory to me (hcf@jlab.org). Alter-
1866 natively, you may create a tarball or a compressed
1867 archive file of your subsection directory and email that
1868 to me. It's your choice. Send me your bib_items.tex file
1869 if you added references to it.

1870 **Update 31-Jul-2018:** Immediately below, I have in-
1871 serted a few drawings and photographs from my own
1872 collection. Feel free to include them in your section if
1873 they are useful. I will remove this entire preamble, in-
1874 cluding unused images, when the paper nears comple-
1875 tion.

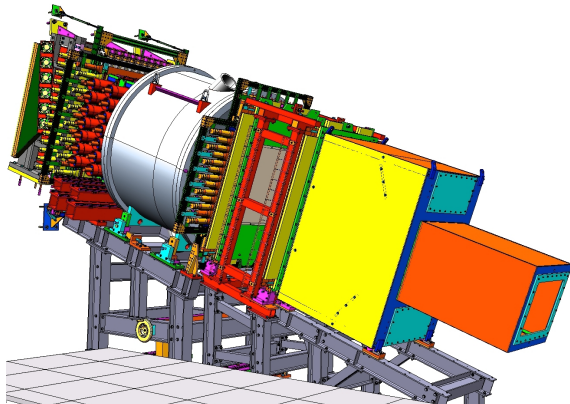


Figure 31: CAD Rendering of SHMS Detector Stack



Figure 32: Photo of the SHMS Detectors in the Shield House

Table 5: Threshold momenta P_{Th} for Čerenkov radiation for charged muons, pions, kaons, and protons in aerogel of four refractive indices ranging from $n=1.011$ to 1.030 .

Particle	P_{Th} $n=1.030$	P_{Th} $n=1.020$	P_{Th} $n=1.015$	P_{Th} $n=1.011$
μ	0.428	0.526	0.608	0.711
π	0.565	0.692	0.803	0.935
K	2.000	2.453	2.840	3.315
p	3.802	4.667	5.379	6.307

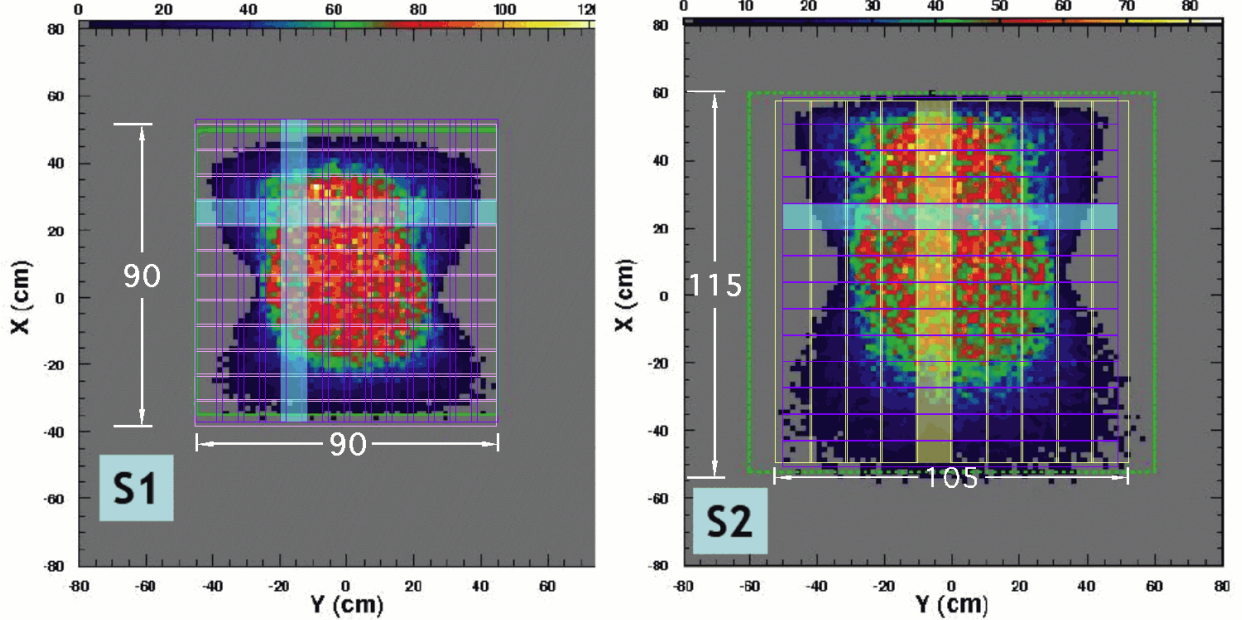


Figure 34: Monte Carlo projection of the particle distribution at two locations in the SHMS detector stack. Studies like this one were used to determine the required sensitive areas of each detector.



Figure 33: One of the SHMS Drift Chamber Cathode Planes being handled during construction

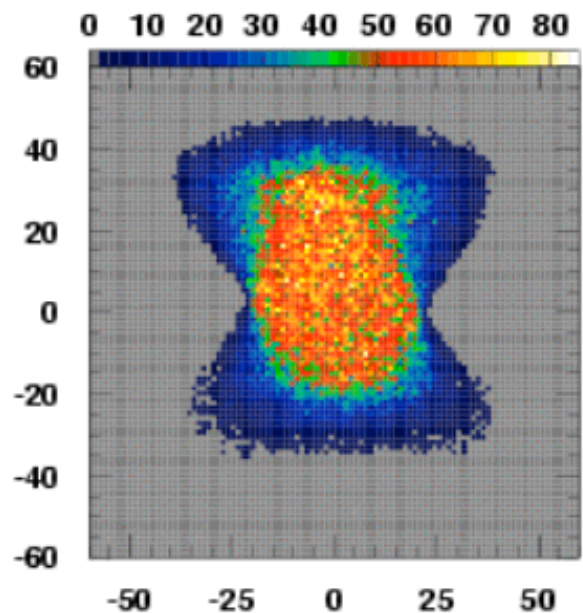


Figure 35: Monte Carlo projection of the particle distribution at the second Drift Chamber. Studies like this one were used to determine the required sensitive areas of each detector.

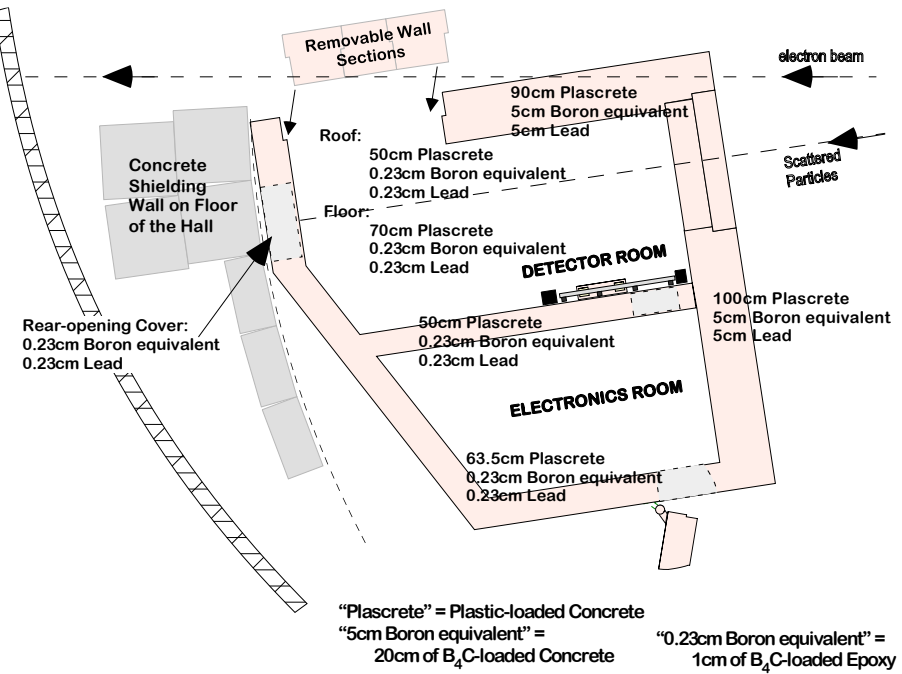


Figure 38: Shielding Arrangement for the SHMS



Figure 36: Photo showing a cross section of the Shield House Wall highlighting the layers of custom materials used.

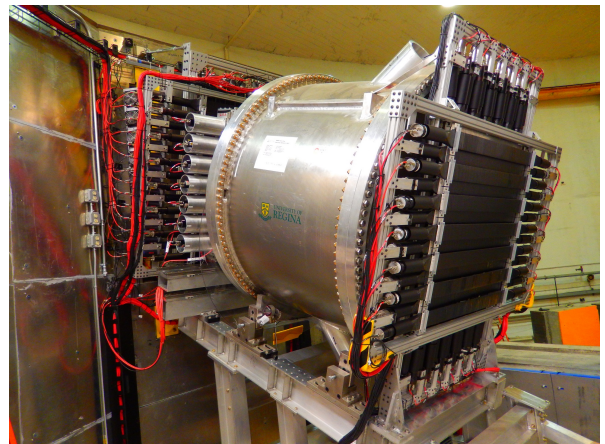


Figure 37: Photo of the SHMS Detectors starting with S1XY

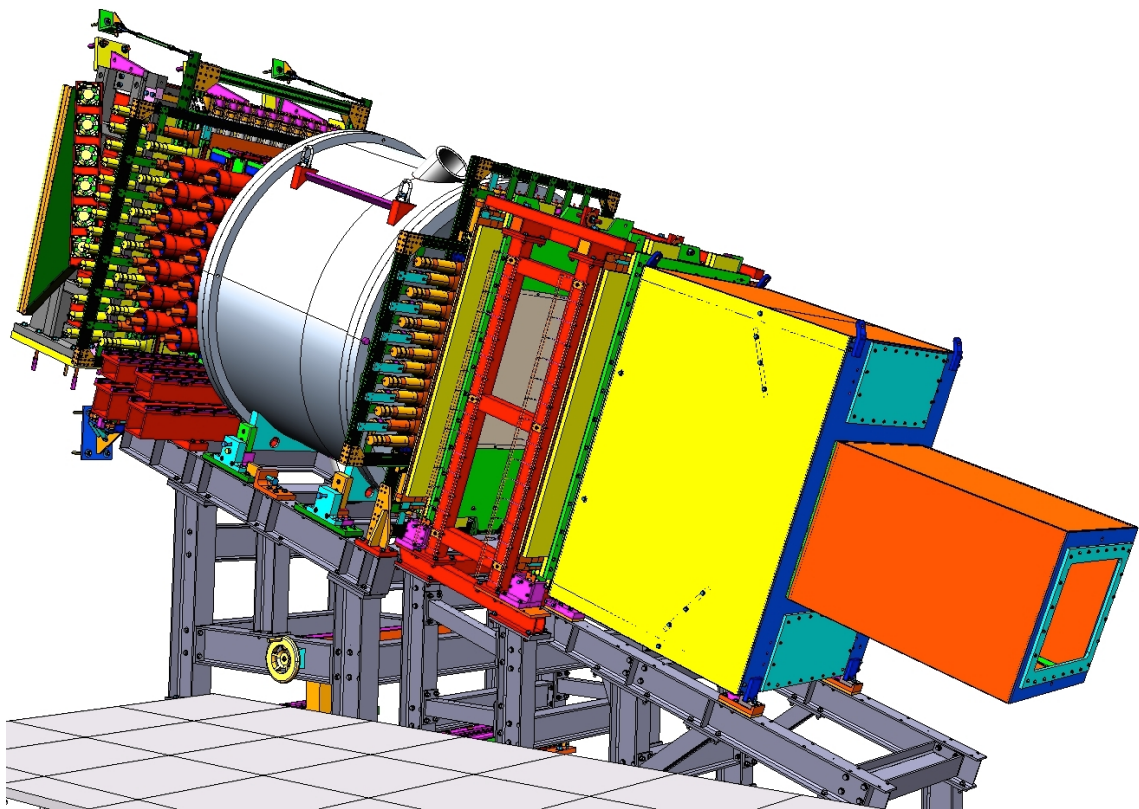


Figure 43: CAD Rendering of SHMS Detector Stack

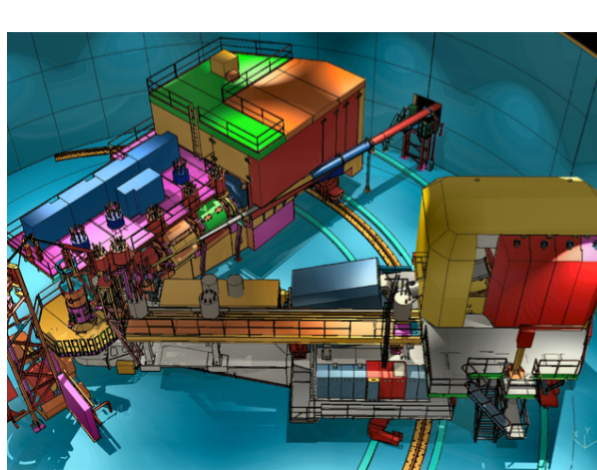


Figure 39: CAD Rendering of the SHMS and the HMS in Hall C

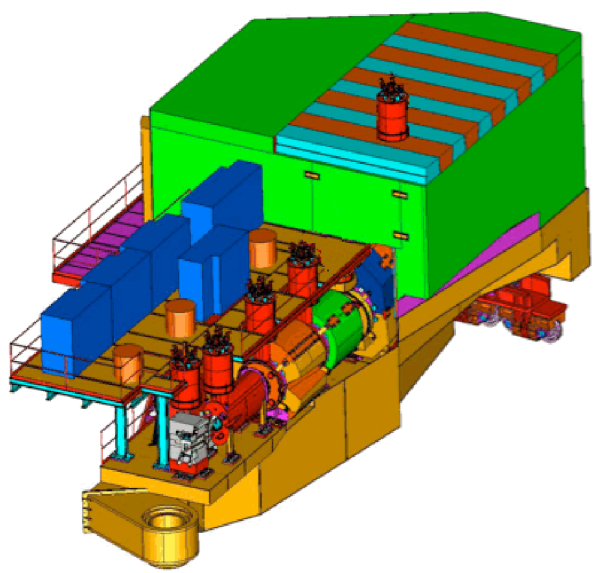


Figure 40: CAD Rendering of the SHMS

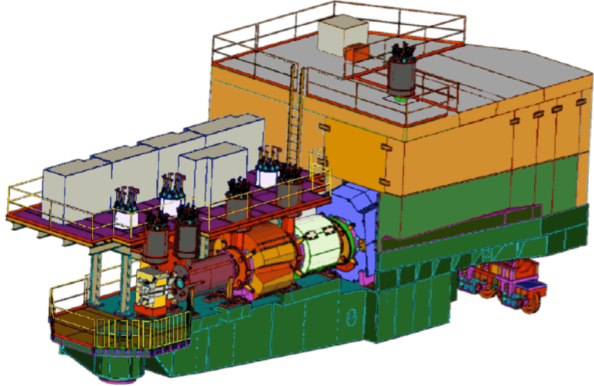


Figure 41: CAD Rendering of the SHMS in colors approximating those actually used.

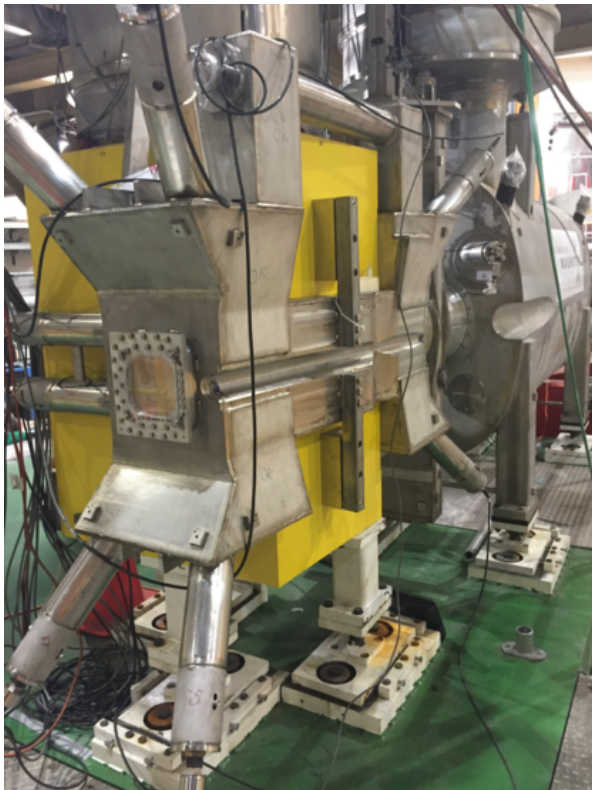


Figure 42: The Horizontal-Bend Magnet, which acts as a septum to bend scattered particles 3° away from the electron beam. The square flange on the front of the magnet surrounds the entrance vacuum window, while the slot along the near side allows the beamline vacuum pipe to come within 5.5° of the magnet axis.

Table 6: An old table of power supply settings used as an example of creating a table.

Detector Element	Heavily Ionizing		Minimum Ionizing Tracks	
	Left Half	Right Half	Left Half	Right Half
HVPS-C	4550	4350	4950	4750
HVPS-G	3050	2850	3450	3250
Window	0	0	0	0
Cathode	4532	4329	4931	4729
GEM-1i	2869	2656	3242	3026
GEM-1o	2579	2374	2915	2705
GEM-2i	2087	1918	2359	2185
GEM-2o	1798	1642	2031	1871
GEM-3i	1143	1040	1292	1185
GEM-3o	845	764	955	871
Padboard	0	0	0	0